5 Post-processing methods for passivity enforcement

Computer Methods in Applied Mechanics and Engineering 418 (2024) 116495

Contents lists available at ScienceDirect

Comput. Methods Appl. Mech. Engrg.

journal homepage: www.elsevier.com/locate/cma

An efficient isogeometric/finite-difference immersed boundary method for the fluid–structure interactions of slender flexible structures

Vishal Agrawal [a,b,*], Artem Kulachenko [a], Nicolò Scapin [b], Outi Tammisola [b], Luca Brandt [b,c]

[a] Solid Mechanics, Department of Engineering Mechanics, KTH Royal Institute of Technology, Stockholm, Sweden
[b] FLOW, Department of Engineering Mechanics, KTH Royal Institute of Technology, Stockholm, Sweden
[c] Department of Energy and Process Engineering, Norwegian University of Science and Technology, Trondheim, Norway

ARTICLE INFO

Keywords:
Fluid–structure interactions
Partitioned solvers
Geometrically exact beam model
Isogeometric analysis
Incompressible flows
Immersed-boundary method

ABSTRACT

In this contribution, we present a robust and efficient computational framework capable of accurately capturing the dynamic motion and large deformation/deflection responses of highly-flexible rods interacting with an incompressible viscous flow. Within the partitioned approach, we adopt separate field solvers to compute the dynamics of the immersed structures and the evolution of the flow field over time, considering finite Reynolds numbers. We employ a geometrically exact, nonlinear Cosserat rod formulation in the context of the isogeometric analysis (IGA) technique to model the elastic responses of each rod in three dimensions (3D). The Navier–Stokes equations are resolved using a pressure projection method on a standard staggered Cartesian grid. The direct-forcing immersed boundary method is utilized for coupling the IGA-based structural solver with the finite-difference fluid solver. In order to fully exploit the accuracy of the IGA technique for FSI simulations, the proposed framework introduces a new procedure that decouples the resolution of the structural domain from the fluid grid. Uniformly distributed Lagrangian markers with density relative to the Eulerian grid are generated to communicate between Lagrangian and Eulerian grids consistently with IGA. We successfully validate the proposed computational framework against two- and three-dimensional FSI benchmarks involving flexible filaments undergoing large deflections/motions in an incompressible flow. We show that six times coarser structural mesh than the flow Eulerian grid delivers accurate results for classic benchmarks, leading to a major gain in computational efficiency. The simultaneous spatial and temporal convergence studies demonstrate the consistent performance of the proposed framework, showing that it conserves the order of the convergence, which is the same as that of the fluid solver.

1. Introduction

Interactions between slender flexible structures and a fluid flow can be found in many engineering and biological applications. A few examples are the paper-making process [1,2], a flag fluttering in the wind [3,4], flapping of insects wings and swimming of aquatic animals/microorganisms [5–7]. However, it is quite challenging to capture the complex interactions between an array of flexible structures and the surrounding fluid flow through numerical simulations. It requires a well-posed formulation for the

* Corresponding author at: Solid Mechanics, Department of Engineering Mechanics, KTH Royal Institute of Technology, Stockholm, Sweden.
E-mail addresses: vishala@kth.se, agrawalvishal34@gmail.com (V. Agrawal).

https://doi.org/10.1016/j.cma.2023.116495
Received 12 June 2023; Received in revised form 24 August 2023; Accepted 27 September 2023
Available online 17 October 2023

motion and change in the geometry of the structures, especially when they undergo large deflections due to the forces exerted by the surrounding fluid and the simultaneous modifications of the flow induced by the flexible structures over time. Over the last few decades, various numerical methods have been introduced, providing effective means for understanding the underlying physics in the interactions between elastic structures and incompressible flow. These methods mainly differ in the temporal and spatial approaches used for the coupling of the fluid and structure domains, see [8–10].

For temporal coupling, either a monolithic or partitioned approach is utilized. In the monolithic approach, the discrete equations for the fluid flow and the structure motion are treated by a single combined solver. On the other hand, the partitioned approach employs separate solvers for the fluid and structure domains, utilizing an appropriate scheme for their coupling. Since the partitioned approach provides the possibility of using the most-matured robust and efficient solvers for the fluid and structure, it has been employed in most FSI applications. In this, the discrete equations for fluid flow and structure motion are integrated in time either in a fully explicit or semi-explicit fashion. However, due to the time-staggering of both solvers, the coupling can become numerically unstable when the structure-to-fluid density ratio is low, invoking the need for appropriate coupling procedures [11,12]. An alternative is to consider iterative strategies that solve the fluid and structure domains repeatedly at each time step until the coupling condition satisfies a certain convergence criterion at the interface. Although such an iterative procedure ensures coupling stability over time, it requires significant computational efforts, which may not be ideal for FSI problems involving many structures. On the other hand, a monolithic approach inherently provides coupling stability in time as there is no time difference between the fluid flow and structure motion. However, it poses a numerical challenge that the single system of combined equations must be well-conditioned, which is not a trivial task from the monolithic formulation viewpoint [13,14].

In addition to the temporal coupling, the spatial coupling of the fluid and structure parts is a key component of every FSI formulation. In this direction, the arbitrary Lagrangian–Eulerian (ALE) method employing boundary-fitted grids is a common technique for representing a structure within the fluid domain, see [15–19]. Although with this approach, the coupling condition can be directly satisfied at the common interface, it is not an optimal choice for the FSI cases involving a large number of structures exhibiting finite deflections. This is because, in such cases, the generation and successive re-adjustment of the boundary-fitted fluid grid become cumbersome and computationally demanding. In addition, each re-meshing step requires mapping the flow field solution from the previous grid to the new one, which may lead to the degradation of the numerical accuracy [20–22].

Due to these reasons, an alternative non-boundary-fitted approach, i.e. the immersed boundary method (IBM) [23], is becoming an increasingly popular choice for FSI cases involving complex-shaped elastic structures with large motion/deformations. The IBM was first introduced by Peskin [23] to study the blood flow around beating heart valves. Since then, numerous variants of immersed boundary approaches have been proposed for different FSI applications, see e.g. [14,24–32]. In boundary methods, the governing equations for fluid flow are solved on a Cartesian Eulerian (background) grid. The equations of motion for a structure are solved on an independent Lagrangian grid. Since the grid of a moving structure almost never coincides with the background fluid grid, the coupling condition at the common interface is enforced by means of a specialized treatment procedure; see [33] for a comprehensive overview. Following the nomenclature of [33], the immersed boundary (IB) procedures are mainly classified into two groups: continuous forcing and direct forcing. The continuous forcing approaches, which are derived from the classical approach proposed by Peskin [23], have been widely used for different FSI applications involving slender structures [34–36]. An advantage of such an approach is that the coupling condition at the interface can be imposed in an exact manner by moving the Lagrangian points on the structure with the background fluid velocity. However, this approach presents some numerical drawbacks for structures with mass and in the employment of a forcing distribution that smears the fluid–structure interface, typically over several grid cells which are in the vicinity of each Lagrangian point. On the other hand, the direct-forcing approach overcomes the drawback of the continuous forcing IB by introducing a body-force term in the fluid flow equations computed from Newton's law of motion, making this approach well-posed for handling structures with mass, and thus has been applied in different FSI applications [37–43]. Although it provides good results for fixed structures, it induces spurious oscillations of the hydrodynamic forces for the moving structures. Successful direct-forcing IB approaches that use improved methods to attenuate the coupling stability stemming from the spurious oscillations of hydrodynamic forces can be found in [44–48].

The aim of the present work is to develop an accurate, robust, and efficient numerical framework for FSI of rod-like flexible structures subjected to a viscous fluid flow. To achieve such a goal, the most-appropriate individual solution techniques for the fluid and structure domains and their coupling are combined together using a partitioned approach. To describe the dynamic mechanical behavior of flexible rods under different loading conditions, we adopt the most general formulation of Simo and Vu-Quoc [49,50], i.e. geometrically exact Cosserat rod model. We utilize this model as (1) it provides a means to describe the three-dimensional (3D) physical behavior of a slender structure with a one-dimensional (1D) mathematical model without any loss of physical correctness. This makes it a computationally attractive and efficient option, particularly for simulating a large number of individual structures [49]. (2) it is mathematically capable of capturing large deflections/bending, rotations, twisting, shearing, and stretching of a rod subjected to a wide range of boundary conditions, cf [49,51–54].

For solving the equations of motion for the Cosserat rod, the isogeometric analysis (IGA) technique is adopted. We resort to IGA as it provides distinct advantageous features such as higher accuracy, stability, and superior convergence properties per degree of freedom (DOF), and direct import of complex-shaped geometries as compared to traditional finite element (FE) approaches [55,56]. Specifically, we start by recalling that the kinematic of slender structures such as cables or rods are mathematically represented by high-order spatial partial differential equations. As a result, the weak form based on the standard Galerkin method of the problem involves the second-order spatial derivatives, requiring basis functions having at least C^1-continuity globally. Due to such requirement, the standard Lagrange polynomial-based FE approximation, which is globally C^0-continuous cannot be applied directly, therefore additional procedures are required to solve this problem. The adoption of the C^1-continuous Hermite polynomial

functions as a basis or the mixed formulation are among the usually preferred approaches. On the other hand, the NURBS-based IGA technique is naturally suited for structural problems as it intrinsically provides higher-continuous NURBS functions as a basis and thus inherently eliminates the requirement of the additional procedure needed in the context of FE. It has been analytically and computationally shown that due to the tailorable inter-element continuity and non-negativeness of the basis functions, the IGA approach is capable of delivering higher accuracy, numerical stability, and robustness per DOF as compared to the traditional FE method in many solid mechanics applications including slender structures [57–59]. In addition, the unified design-to-analysis setting of the IGA technique enables direct analysis on the complex shaped and/or large curvature/pre-twisted geometries as compared to the traditional FE approach, involving an additional (computationally expensive) mesh generation procedure [56]. Besides the above advantages, it is worth mentioning that the IGA technique has proven to be significantly beneficial in terms of accuracy, robustness, and computational efficiency in handling contact between highly flexible geometries. This is because an IGA-based smooth description of the contact surface yields a unique definition of the contact kinematic variables. With this, IGA intrinsically eliminates the computational issues stemming from the standard C^0-continuous FE-based discretization as compared to the standard FE method, which requires additional surface smoothing procedures. Further, since IGA facilitates the contact search in a patch-wise fashion rather than the conventional element-wise manner, it substantially reduces the computational cost associated with the contact search and the corresponding book-keeping task [60,61]. Overall, the geometrically exact rod model implemented in the IGA setting makes the structural solver computationally most suitable for capturing elastic responses of the slender rods under different loading conditions as compared to traditional FE approaches [52,53,62].

For resolving the flow field, the standard second-order finite-difference (FD) method is adopted. We use an FD-based fluid solver due to its algorithmic simplicity, computational efficiency, and applicability to various fluid flow problems at different Reynolds numbers. To couple the interactions between structure motion and underlying fluid flow, the direct-forcing IB method of Uhlmann [44] is adopted as a first step towards designing a simple yet effective computation framework for FSI simulations.

Although the immersed boundary method provides results with reasonable accuracy, it requires an excessively fine structural mesh due to its prominent limitation that the nodal density of the immersed structure must be of the same order as the background fluid grid to avoid any flow leakage [44,63,64]. This not only negates the key advantage of the IGA technique that accurate results can be obtained even with a coarse mesh but also considerably increases the computational cost of FSI simulations, especially when many structures are involved. Here, we thus propose a new procedure that overcomes the earlier-mentioned limitation of the IB method in the context of isogeometric/finite-difference framework without any loss of stability and robustness of the FSI simulations. For this, a large number of uniformly distributed additional Lagrangian markers meeting the relative nodal density requirement of the IB method are generated over a user-defined coarse mesh via spline interpolations. We then interpolate velocity to and spread forces from these Lagrangian markers instead of nodal points of the IGA discretized structure. This clearly enables us to use a significantly coarser structural mesh irrespective of the background Eulerian grid resolution, which constitutes another key ingredient of the presented framework.

In the same spirit, Griffith and Luo [64] have proposed an IB method that enables independent discretization of an FE-discretized structure and the background fluid grid. They used a dynamically adapted Gaussian quadrature rule to construct Lagrangian interaction points on the top of a FE constructed mesh. Since in IGA, the nodal points used to construct a given geometry are usually unevenly distributed and have support in more than one element, an alternative method is needed. In this context, recently, Nitti et al. [31] proposed an isogeometric/finite-difference IB method that decouples the relative nodal density of the shell structure and fluid domain. They performed an adaptive collocation of the Lagrangian markers over an IGA discretized shell with fixed resolution at a given Eulerian grid. However, the method's performance for different/coarsest nodal densities of the structure at a fixed Eulerian grid has not been examined. A few efforts towards applying the geometrically exact model to the structural solver of an FSI framework have also been carried out. In this context, Tschisgale and Fröhlich [65] firstly utilized the finite-difference implementation of the Cosserat rod model in the IBM framework. They proposed a new semi-implicit coupling scheme based on the continuous-forcing IB approach to describe the interactions of flexible structures with fluid. Suguru et al. [66] presented an FSI scheme using the Cosserat rod model with lattice Boltzmann method as a structural solver. Hagmeyer et al. [67,68] proposed two different mixed-dimensional approaches that couples the geometrically exact beam model with Navier–Stokes equations using the GPTS-type and mortar-type coupling approaches within the context of FE method. However, to the best of our knowledge, an FSI framework that couples IGA-based Cosserat rod formulation with the fluid flow equations resolved in the FD environment using an IB procedure enabling independent mesh resolutions for the slender flexible structures and fluid domains has never been proposed. In this work, we develop an isogeometric/finite-difference IB-based numerical framework that is capable of accurately capturing the large deflections/motions of the flexible filaments induced by fluid forces and the evolution of the fluid field over time due to its interaction with the filaments.

The validity of the numerical framework is tested against two numerical examples of increasing complexities: (i) the flapping of a flexible filament in a uniform flow and (ii) the motion of an array of flexible filaments subjected to a pulsating flow in a three-dimensional channel. The performance analysis is presented in terms of accuracy and computational cost for the above two numerical examples. In addition to this, the consistent performance of the developed framework is provided through grid convergence studies. In all cases, satisfactory results are obtained. The proposed approach permits using significantly coarse structural meshes than the background fluid grid without losing numerical stability.

The remaining paper is structured as follows. In Section 2, we briefly describe the mathematical models for the fluid and structure parts and the coupling conditions at the interface. Next, in Section 3, the numerical methods used for solving the governing equations are detailed. We describe the proposed IB procedure in Section 3.3. After that, in sections 4 and 5, we show the validations of the developed framework and demonstrate its performance and efficacy using various numerical examples. Finally, the summary is provided in Section 6 with an indication of the future directions.

2. Governing equations

2.1. Navier–Stokes equations for fluid motion

The dynamics of an unsteady incompressible viscous flow is governed by the three-dimensional (3D) Navier–Stokes and continuity equations. In an inertial Cartesian frame of reference, their non-dimensional form reads

$$\frac{\partial \boldsymbol{u}}{\partial t} + \boldsymbol{\nabla} \cdot (\boldsymbol{u} \otimes \boldsymbol{u}) = -\boldsymbol{\nabla} p + \frac{1}{Re} \nabla^2 \boldsymbol{u} + \boldsymbol{f}\,, \tag{1a}$$

$$\boldsymbol{\nabla} \cdot \boldsymbol{u} = 0\,, \tag{1b}$$

where $\boldsymbol{u} = (u, v, w)^{\mathrm{T}}$ represent the velocity field having components along the coordinate (x, y, z) directions of the fluid-domain, p is the pressure field, and t is the time variable. For our problem, the external forcing term $\boldsymbol{f}$ consists of two parts: an external mass-specific volume force $\tilde{\boldsymbol{f}}$, such as pressure gradient driving the flow, and the coupling force $\bar{\boldsymbol{f}}$ that is used to satisfy the no-slip boundary condition at the fluid–structure interface, described below in Section 3.3. The Reynolds number is given as $Re = \rho U L/\mu$, where ρ denotes the fluid mass density, μ is its dynamic viscosity, and U and L are the characteristic velocity and length scales.

2.2. Cosserat rod model for the slender flexible structures

The structure considered in the present work is a long slender elastic three-dimensional rod whose length is considerably larger than its cross-section. We use a geometrically exact Cosserat rod model to describe the mechanical behavior of the slender rod. It is an appropriate model to capture the motion and finite strains of a deformable rod having different constitutive properties using one-dimensional continua without making any assumptions concerning the rotation [49,51,69]. Due to its computationally efficient advantages in modeling three-dimensional deformable rods, the Cosserat rod model has been applied to a wide range of applications, e.g. in the design and engineering of modeling cables, hair, fibers, and composites. Motivated by the above-mentioned advantages, we use this model for simulating a number of flexible filaments interacting in a viscous fluid. In the following, we outline the Cosserat rod model based on the works [49,51–53,69].

2.2.1. Configuration and parameterization

In the Cosserat rod model, a slender rod of length L is represented by its centerline curve, i.e. the line of its mass centroids, $\boldsymbol{r} : [0, L] \in \mathbb{R}^3$, and the orientation of its rigid cross-section, which is described in terms of the rotation matrix $\boldsymbol{R} : [0, L] \in SO(3)$, see Fig. 1 for an illustration. Here, $\boldsymbol{R}$ is a 3D orthogonal rotation matrix belonging to the special orthogonal group $SO(3)$ in the terminology of Lie algebra, see [70] for a detailed description of the rotation manifold $SO(3)$. At the time t, the line of the mass centroid of the rod is parameterized by a curvilinear abscissa $s \in [0, L]$ such that $\boldsymbol{r} = \boldsymbol{r}(s, t)$, and the cross-section's orientation with $\boldsymbol{R} = \boldsymbol{R}(s, t)$. Among the popular choices: Euler angles, Rodrigues' rotation, and axis-angle representation, we use the unit-length quaternions, i.e. $q = [q_1, q_2, q_3, q_4]^{\mathrm{T}} \in \mathbb{R}^4$ and $\|q\| = 1$, for parameterizing $\boldsymbol{R}$. Quaternions avoid the gimbal lock effect and are computationally efficient [49,71]. The quaternion-parameterized rotation matrix reads as

$$\boldsymbol{R}(\boldsymbol{q}) = \begin{bmatrix} q_1^2 + q_2^2 - q_3^2 - q_4^2 & 2(q_2 q_3 - q_4 q_1) & 2(q_2 q_4 + q_3 q_1) \\ 2(q_2 q_3 + q_4 q_1) & q_1^2 - q_2^2 + q_3^2 - q_4^2 & 2(-q_2 q_1 + q_3 q_4) \\ 2(q_2 q_4 - q_3 q_1) & 2(q_2 q_1 + q_3 q_4) & q_1^2 - q_2^2 - q_3^2 + q_4^2 \end{bmatrix}. \tag{2}$$

Since the centerline of the rod is parameterized in terms of the curvilinear abscissa s, the quaternions and its corresponding rotation matrix are represented in the same fashion, i.e. $\boldsymbol{R} = \boldsymbol{R}(\boldsymbol{q}(s))$.

2.2.2. Strains and stresses

Based on the centerline curve $\boldsymbol{r}(s)$ and the orientation of the cross-section $\boldsymbol{R}(s)$ at s, the internal translatory strain in the rod is measured by

$$\bar{\boldsymbol{\varepsilon}} = \boldsymbol{R}^{\mathrm{T}} \boldsymbol{r}' - \mathbf{e}_3\,, \tag{3}$$

where $\boldsymbol{r}' = \frac{\mathrm{d}\boldsymbol{r}}{\mathrm{d}s}$ represents the gradient along the rod center and $\mathbf{e}_3$ denotes the Cartesian basis vector $\{1, 0, 0\}^{\mathrm{T}}$. For the initial or undeformed configuration of the rod $\bar{\boldsymbol{\varepsilon}} = \mathbf{0}$, thus $\boldsymbol{R}^{\mathrm{T}} \boldsymbol{r}' = \mathbf{e}_3$. Further, the components of $\bar{\boldsymbol{\varepsilon}}$, i.e. $\bar{\varepsilon}_1$ refers to axial strain, while $\bar{\varepsilon}_2$ and $\bar{\varepsilon}_3$ indicate shear strains.

The internal rotational strain of the rod is measured by computing the relative orientation between adjacent cross-sections as in the following [52,53]

$$[\bar{\boldsymbol{\kappa}}]_{\times} = \boldsymbol{R}^{\mathrm{T}} \boldsymbol{R}'\,, \tag{4}$$

where $\boldsymbol{R}' = \frac{\mathrm{d}\boldsymbol{R}}{\mathrm{d}s}$, and $[\bar{\boldsymbol{\kappa}}]_{\times}$ denotes skew-symmetric matrix of $\bar{\boldsymbol{\kappa}}$ such that $[\bar{\boldsymbol{\kappa}}]_{\times} \cdot \boldsymbol{u} = \bar{\boldsymbol{\kappa}} \times \boldsymbol{u}$ for a vector $\boldsymbol{u} \in \mathbb{R}^3$. The components of $\bar{\boldsymbol{\kappa}}$, i.e. $\bar{\kappa}_1$ represents the torsional curvature, while $\bar{\kappa}_2$ and $\bar{\kappa}_3$ the bending curvatures. Further, if the initial configuration of the rod is pre-stretched or curved, the effective translatory and rotational strains in the rod are

$$\boldsymbol{\varepsilon} = \bar{\boldsymbol{\varepsilon}} - \boldsymbol{\varepsilon}_0\,, \qquad \boldsymbol{\kappa} = \bar{\boldsymbol{\kappa}} - \boldsymbol{\kappa}_0\,, \tag{5}$$

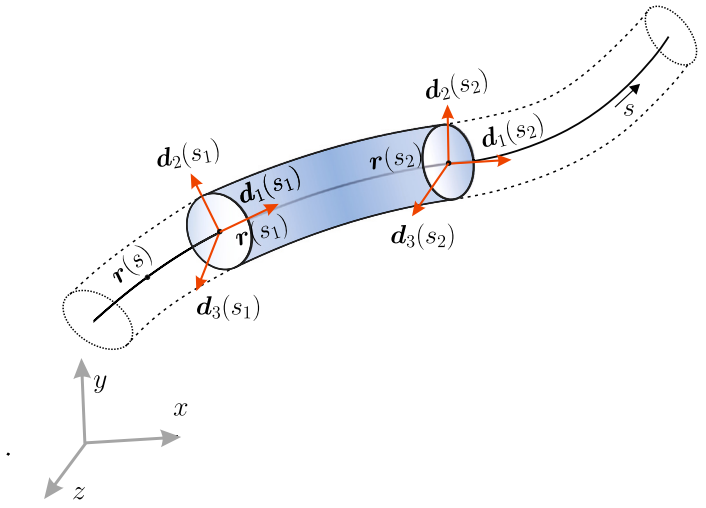

Fig. 1. Schematic of a Cosserat rod: It is represented by its centerline curve $\boldsymbol{r}(s)$ and the orientation of the cross-section along the rod. The latter is described by three-dimensional orthonormal direction vectors: $\boldsymbol{d}_1(s)$, $\boldsymbol{d}_2(s)$ and $\boldsymbol{d}_3(s)$, which combinedly results in a rotation matrix $\boldsymbol{R}(s) = [\boldsymbol{d}_2(s), \boldsymbol{d}_3(s), \boldsymbol{d}_1(s)]$. (For interpretation of the references to colour in this figure legend, the reader is referred to the web version of this article.)

where $\boldsymbol{\epsilon}_0$ and $\boldsymbol{\kappa}_0$ denote the strains arising from the pre-stretching or curved configuration of the rod at $t = 0$, and are determined using Eqs. (3) and (4), respectively.

Based on the two nonlinear strain vectors defined in Eqs. (3) and (4), the translatory and rotational stresses are

$$\hat{\boldsymbol{n}} = \mathbf{C}\boldsymbol{\epsilon}, \qquad \hat{\boldsymbol{m}} = \mathbf{D}\boldsymbol{\kappa} \tag{6}$$

for the linear elastic constitutive law. In the above equation, the intrinsic material matrices are defined as $\mathbf{C} = \mathrm{diag}[EA, GAk_y, GAk_z]$ and $\mathbf{D} = \mathrm{diag}[GJ, EI_{yy}, EI_{zz}]$, with Young's modules E, shear modulus G, torsion correction factors k_y and k_z, second moment of areas I_{yy} and I_{zz}, and $J = I_{yy} + I_{zz}$ along the y, z, and x-axis of the beam. It is noted that the stresses in Eq. (6) are expressed in the local coordinate system of the rod. They can be easily rotated from the local to the global Euclidiean coordinate frame with

$$\boldsymbol{n}_{\mathrm{int}} = \boldsymbol{R}\hat{\boldsymbol{n}}, \qquad \boldsymbol{m}_{\mathrm{int}} = \boldsymbol{R}\hat{\boldsymbol{m}}\,, \tag{7}$$

where $\boldsymbol{n}_{\mathrm{int}}$ and $\boldsymbol{m}_{\mathrm{int}}$ are referred to as internal force and moment, respectively. With the expressions above, the rotation matrix transforms internal forces and moments from their spatial to material configurations.

2.2.3. The equations of motion of the Cosserat rod

The strong form of the linear and angular momentum balance equations for the geometrically exact Cosserat rod can be written in the material or initial form as [49,51]:

$$\begin{aligned} \rho_s A\ddot{\boldsymbol{r}}(s,t) &= \boldsymbol{n}'_{\mathrm{int}}(s,t) + \boldsymbol{n}_{\mathrm{ext}}(s,t)\,, \\ \rho_s \boldsymbol{I}\dot{\boldsymbol{\omega}}(s,t) + \boldsymbol{\omega}(s,t)\times\rho_s\boldsymbol{I}\boldsymbol{\omega}(s,t) &= \boldsymbol{m}'_{\mathrm{int}}(s,t) + \boldsymbol{r}'(s,t)\times\boldsymbol{n}_{\mathrm{int}}(s,t) + \boldsymbol{m}_{\mathrm{ext}}(s,t)\,. \end{aligned} \tag{8}$$

In the above, the first equation corresponds to the temporal evolution of the centerline curve of the rod in terms of $\boldsymbol{r}(s,t)$, while the second equation describes the temporal evolution of the rotation of the cross-sections along the arc-length coordinate s. They hold $\forall s \in (0, L)$ and $t \in (0, T)$. The spatial and temporal derivatives of the various terms are defined as $\dot{\square} = \mathrm{d}\square/\mathrm{d}t$, $\ddot{\square} = \mathrm{d}^2\square/\mathrm{d}t^2$, and $\square' = \partial\square/\partial s$. In the above equations, ρ_s denotes the mass density of the rod, A is its cross-section area, $\boldsymbol{I}$ is the moment of area tensor, and $\boldsymbol{\omega}$ is the angular velocity of A in the global frame. Moreover, $\boldsymbol{n}_{\mathrm{ext}}$ and $\boldsymbol{m}_{\mathrm{ext}}$ are prescribed externally distributed (line) forces and moments acting on the rod surface. Note that the externally prescribed force consists of two parts, (1) the force due to gravity $(\rho_s - \rho)A\mathbf{g}$ with gravitation acceleration $\mathbf{g}$, and (2) the external fluid loads acting on the interface between the fluid and structure, denoted as $\bar{\boldsymbol{n}}_{\mathrm{ext}}$ and $\bar{\boldsymbol{m}}_{\mathrm{ext}}$. We describe such forces and their computations in Section 3.3 below.

2.3. Fluid–structure coupling conditions

The Navier–Stokes Eqs. (1) and the Cosserat rod Eqs. (8) form a system of differential equations, and the physical coupling between the fluid phase and the immersed structure is realized by enforcing the *no-slip* and *dynamic forcing* conditions at the interface Γ. The no-slip condition implies that the fluid moves with the same velocity as the surface of the structure. Mathematically, it is expressed as

$$\boldsymbol{u} = \boldsymbol{w}(\boldsymbol{x}, t) \qquad \text{for} \quad \boldsymbol{x} \in \Gamma\,, \tag{9}$$

where $\boldsymbol{w}(\boldsymbol{x},t)$ denotes the velocity of a point on the moving structure surface Γ. For the Cosserat rod $\boldsymbol{w}=\dot{\boldsymbol{x}}$, where $\dot{\boldsymbol{x}}=\boldsymbol{r}+\boldsymbol{R}\cdot\boldsymbol{\zeta}_0$. With this, Eq. (9) can be rewritten in terms of its translatory and rotational contributions as

$$\boldsymbol{u}=\dot{\boldsymbol{r}}+\boldsymbol{\omega}\times\boldsymbol{\zeta} \qquad \text{for} \quad \boldsymbol{x}\in\Gamma\,. \tag{10}$$

Here, $\boldsymbol{\zeta}=\boldsymbol{x}-\boldsymbol{r}$ denotes the position of the rod surface point $\boldsymbol{x}\in\Gamma$ with respect to its centerline $\boldsymbol{r}$ in the local coordinate frame. The dynamic coupling condition enforces that the surface-specific forces exerted by the fluid and immersed structure are in equilibrium at the interface Γ. For this condition, the coupling forces are introduced in the momentum balance Eq. (1a) of the fluid and governing Eq. (8) of the structure.

3. Discretizations of the fluid and solid equations

3.1. Spatial and temporal discretization of the fluid equations

We use a standard second-order finite-difference method for the spatial discretization of the Navier–Stokes Eqs. (1) on a fixed, equidistant staggered Cartesian grid. In the staggered arrangement, the pressure and density are stored at the cell center, and the velocity components are located at the cell faces. This avoids the checkerboard oscillation of the pressure field [72]. The flow Eqs. (1) are coupled with a fractional step pressure projection method [73,74], and their time integration is accomplished by a fully explicit three-step low-storage Runge–Kutta scheme (RK3) [75,76]. The advancement of the discretized flow equations for the rth $=1,2,3$ RK3 sub-step reads

$$\frac{\tilde{\boldsymbol{u}}-\boldsymbol{u}^r}{\Delta t}=\alpha_r\mathbf{AD}^r+\beta_r\mathbf{AD}^{r-1}-\gamma_r\nabla p^{r-1/2}+\tilde{\boldsymbol{f}}\,, \tag{11a}$$

$$\bar{\boldsymbol{u}}=\tilde{\boldsymbol{u}}+\Delta t\bar{\boldsymbol{f}} \tag{11b}$$

$$\nabla^2\tilde{p}=\frac{\boldsymbol{\nabla}\cdot\bar{\boldsymbol{u}}}{\gamma_r\Delta t}\,, \tag{11c}$$

$$\boldsymbol{u}^{r+1}=\tilde{\boldsymbol{u}}-\gamma_r\Delta t\boldsymbol{\nabla}\tilde{p}\,, \tag{11d}$$

$$p^{r+1/2}=p^{r-1/2}+\tilde{p}\,. \tag{11e}$$

In the above equations, the sub-step $r=1$ corresponds to time level t_n and $r=3$ to t_{n+1}, $\tilde{\boldsymbol{u}}$ is the predicted fluid velocity, and $\mathbf{AD}=-(\boldsymbol{u}\cdot\nabla)\boldsymbol{u}+\nu\nabla^2\boldsymbol{u}$. Further, $\tilde{\boldsymbol{f}}$ is the mass-specific volume force, and $\tilde{p}$ is the pressure correction [73,77]. In Eq. (11b), the fluid velocity $\tilde{\boldsymbol{u}}$ is updated with the fluid–structure coupling force $\bar{\boldsymbol{f}}$, arising from the immersed boundary treatment described in Section 3.3. It makes the fluid motion constraint by the immersed boundary interface. The coefficients of the RK3 scheme for the r^{th} step are given by $\alpha_r=[8/1,\,5/12,\,3/4]$, $\beta_r=[0,\,-17/60,\,-5/12]$, and $\gamma_r=\alpha_r+\beta_r$ [76]. The pressure correction field $\tilde{p}$ is computed by solving the second-order finite difference Poisson Eq. (11c), using a fast Fourier transform (FFT)-based solver [78]. It is thereafter used to project the predicted velocity $\tilde{\boldsymbol{u}}$ onto the divergence-free space to satisfy the incompressibility constraint (1b). For the numerical stability of the Runge–Kutta scheme, the following criteria is used [76]:

$$\Delta t<\min\left(\frac{1.65\Delta k^2}{12\nu},\,\frac{\sqrt{3}\Delta k}{\sum_{i=1}^{3}|u_i^r|}\right) \tag{12}$$

where $\Delta k=\min(\Delta x,\Delta y,\Delta z)$ and $\nu=\mu/\rho$ is the kinematic viscosity of the fluid. The computational domain considered in this work has dimensions, i.e. $\Omega=[0,L_x]\times[0,L_y]\times[0,L_z]$, where L_x, L_y, and L_z represent the length of the domain along the x, y, and z-direction.

Further, the simulations of the unsteady viscous incompressible flows are performed using open-source code FluTAS[1], see Crialesi-Esposito et al. [79] for the implementation details. It employs a highly-scalable 2DECOMP&FTT library (Li and Lizat [80]), which uses a message-passing interface for the parallelization of the computational domain.

3.2. Discretization of governing equations of the rod using IGA

The isogeometric analysis (IGA) technique, introduced by Hughes et al. (2005) [55], uses computer-aided-design (CAD) polynomial functions, e.g. B-splines, non-uniform rational B-splines (NURBS), etc., as a basis for the construction of a given geometry and for the approximation of the solution space. It has been shown that IGA offers efficient, accurate, and stable simulations for different classes of problems, especially those involving geometries with large curvature and undergoing finite deformations, as compared to the traditional C^0-continuous Lagrange polynomial-based finite element (FE) approach. This is because the higher-continuous polynomial functions lead to a significantly better approximation of the solution space at a fixed mesh than the traditional FE approach, see e.g. [55,56].

In the following, we first present a brief introduction to the NURBS functions, their usage in the constructing of a curve, and different refinement strategies that are used within the framework of IGA in 3.2.1. In Section 3.2.2, we present the NURBS-based parameterization and interpolation of the centerline curve and cross-section orientation of the Cosserat rod. Finally, in Section 3.2.3, we present the NURBS-based discretization of the equation of motion of the rod in the IGA setting based on [49,53].

[1] https://github.com/Multiphysics-Flow-Solvers/FluTAS

3.2.1. NURBS functions, curve, and refinement strategies

For a given vector $\Xi(\xi)$ defined along the ξ parametric direction, a pth order uni-variate, piecewise B-spline function is defined with the following Cox de Boor recursive relation [81]

$$N_{i,0}(\xi) = \begin{cases} 1, & \text{if } \xi_i \le \xi < \xi_{i+1} \\ 0, & \text{otherwise,} \end{cases} \qquad N_{i,p}(\xi) = \frac{\xi - \xi_i}{\xi_{i+p} - \xi_i} N_{i,p-1} + \frac{\xi_{i+p+1} - \xi}{\xi_{i+p+1} - \xi_{i+1}} N_{i+1,p-1}\,, \tag{13}$$

where $\Xi = \{\xi_0, \xi_1, \dots, \xi_{n+p}, \xi_{n+p+1}\}$ contains $(n+p+1)$ parametric coordinates $\xi \in \mathbb{R}$ in an increasing order. One of the most beneficial features of these functions is that a pth-order B-spline function offers C^{p-1} continuous derivatives at any (non-repeated) parametric point. Moreover, they also show non-negativeness at a given point ξ, i.e. $N_{i,p}(\xi) \ge 0$, $\forall s$, and have partition of unity property, i.e. $\sum_{i=1}^{n} N_{i,p}(\xi) = 1$.

Non-uniform rational B-splines (NURBS) are the rationale of the B-spline functions and use additional weight w_i, where $i = 1, \dots, n$. A pth-order NURBS function is defined as [81]:

$$R_i^p(\xi) = \frac{w_i\, N_{i,p}(\xi)}{\sum_{j=1}^{n} N_{j,p}(\xi) w_j}\,, \tag{14}$$

Since NURBS are built using B-splines, they share the same properties, and for $w_i = 1$, $\forall i = 1, \dots, n$, NURBS reduces to B-splines. Thus, we will mainly use the term NURBS in the following. For a given set of control points $\boldsymbol{x}_i = \{x_i, y_i, z_i, w_i\}$, where $i = 1, \dots, n$, a p^{th}-order NURBS curve is constructed using the following linear combination

$$\boldsymbol{c}(\xi) = \sum_{i=1}^{n} R_{i,p}(\xi)\, \boldsymbol{x}_i\,. \tag{15}$$

One of the key advantages of using NUBRS is that the constructed geometries can be refined in a straightforward manner while keeping the original shape and parameterization of the geometry. For a given NURBS geometry, any additional number of elements can be introduced using the *knot insertion* refinement strategy. In this, the insertion of an additional point ξ_j between an existing $[\xi_i, \xi_{i+1}]$ element, splits it into two: $[\xi_i, \xi_j]$ and $[\xi_j, \xi_{i+1}]$, and thus, creates a new element. Another option of refinement is the *order elevation* strategy. In this, as the name implies, the interpolation order of the NURBS functions can be raised from p to $p+1$ or more, while each entry ξ_i in the knot vector is repeated once or according to order elevation strategy to maintain the C^{p-1} continuity of the NURBS functions. The third option of refinement is referred to as the k-refinement. In this, the knot insertion strategy is applied subsequently to the order elevation. It is used to increase the continuity of the NURBS functions and mesh refinement in a simultaneous manner. For further details on this topic, we refer to the monograph by Cottrell et al. [56] and Agrawal and Gautam [82] for implementation details.

3.2.2. Parameterization and interpolation of rod model

We use NURBS for the representation of the Cosserat rod. Each control point associated with the centerline curve contains the position vector $\boldsymbol{x}_i \in \mathbb{R}^3$ and the orientation of its cross-section in terms of unit length quaternions $\boldsymbol{q}_i \in \mathbb{R}^4$: $\{\boldsymbol{x}_i, \boldsymbol{q}_i\}$, as illustrated in Fig. 2. For the given interpolation order p and knot vector $\Xi = \{\xi_0, \dots, \xi_{n+p+1}\}$ defined along the parametric direction, the NURBS-based parameterization of the centerline curve and its derivative are given by

$$\begin{aligned} \boldsymbol{r}(s) &= \sum R_{i,p}(s)\, \boldsymbol{x}_i\,, \qquad \text{and} \\ \boldsymbol{r}'(s) &= \frac{d\boldsymbol{r}(\xi)}{d\xi}\frac{d\xi}{ds} \\ &= \sum R'_{i,p}(\xi)\, \boldsymbol{x}_i\, J_{s\xi}^{-1}\,, \end{aligned} \tag{16}$$

where $d\boldsymbol{r}(\xi)/d\xi$ is the derivative w.r.t to the parametric space ξ, and the Jacobian $J_{s\xi} = \dfrac{\mathrm{d}s}{\mathrm{d}\xi}$ enables the transformation from the spline parametric space ξ to the arc-length abscissa s. With the above expressions, the translational strain $\bar{\boldsymbol{\varepsilon}}$ defined in Eq. (3) can be straightforwardly computed. The interpolation of the cross-section's rotation is done using the exponential map of the weighted sum of the rotation vectors represented in terms of quaternions using the following expression [53]:

$$\boldsymbol{q}(s) = \bar{\boldsymbol{q}} \exp\left(\text{pure} \sum R_{i,p}(s)\, \text{imag}(\log(\bar{\boldsymbol{q}}^*(s)\, \boldsymbol{q}_i))\right)\,. \tag{17}$$

Here, $\bar{\boldsymbol{q}}(s)$ denotes an average of the rotation of the closest $p+1$ nodes at s and $\bar{\boldsymbol{q}}\,*$ is the quaternion conjugate of $\bar{\boldsymbol{q}}$. Once $\boldsymbol{q}(s)$ is computed, the rotation matrix $\boldsymbol{R}$ can be evaluated as $\boldsymbol{R}(\boldsymbol{q})$. Finally, the curvature strain $\boldsymbol{\kappa}(s)$ is computed with [53]

$$\boldsymbol{\kappa}(s) = \sum_{i}^{p+1} J_{s\xi}^{-1}\, \boldsymbol{R}'_{i,p}(s)\, [\text{imag}(\log(\bar{\boldsymbol{q}}^*(s)\, \boldsymbol{q}_i))]\,. \tag{18}$$

3.2.3. Discretization of rod equations using IGA

The variational form of the dynamic equation of motion of the rod can be derived by multiplying any arbitrary admissible variation $\delta\boldsymbol{\eta} = (\delta\boldsymbol{r}(s), \delta\boldsymbol{\theta}(s))$ to the equations of the linear and angular momentum Eq. (8), and integrating the equation over the length of the rod. The final expression for the variational form can be expressed as the sum of the following two terms [49,51]:

$$G := G_{\text{dyn}} + G_{\text{stat}} \tag{19}$$

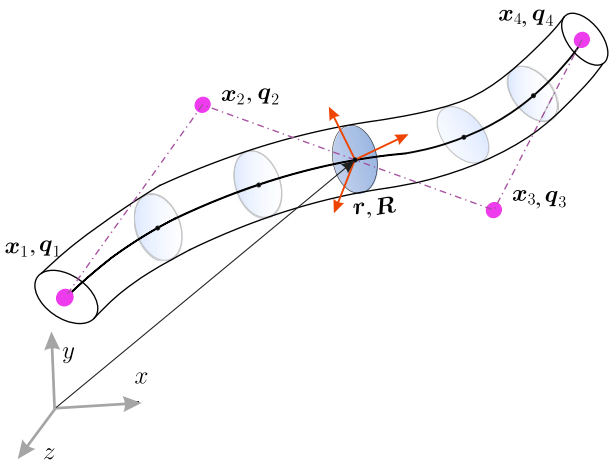

Fig. 2. Spline-based discretization of a Cosserat rod. The control points' position and rotational degree of freedom are represented by x_i, q_i, with $i = 1, \ldots, 4$. The spline interpolated position of a centerline point and the orientation of the cross-section are indicated by r, R. (For interpretation of the references to colour in this figure legend, the reader is referred to the web version of this article.)

given as

$$G_{\text{dyn}} = \int_0^L \left[\rho_s A \ddot{\boldsymbol{r}} \cdot \delta \boldsymbol{r}(s) + (\rho_s \boldsymbol{I} \cdot \dot{\boldsymbol{\omega}} + \boldsymbol{\omega} \times \rho_s \boldsymbol{I} \cdot \boldsymbol{\omega}) \cdot \boldsymbol{\theta}(s) \right] ds \tag{20}$$

$$G_{\text{stat}} = \int_0^L \begin{bmatrix} \boldsymbol{n}_{\text{int}} \\ \boldsymbol{m}_{\text{int}} \end{bmatrix} \cdot \begin{bmatrix} \boldsymbol{I} \dfrac{d}{ds} & [\boldsymbol{r}']_\times \\ \boldsymbol{0} & \boldsymbol{I} \dfrac{d}{ds} \end{bmatrix}^{\mathrm{T}} \cdot \begin{bmatrix} \delta \boldsymbol{r} \\ \delta \boldsymbol{\theta} \end{bmatrix} ds - \int_0^L \begin{bmatrix} \boldsymbol{n}_{\text{ext}} \\ \boldsymbol{m}_{\text{ext}} \end{bmatrix} \cdot \begin{bmatrix} \delta \boldsymbol{r} \\ \delta \boldsymbol{\theta} \end{bmatrix} ds \tag{21}$$

The NURBS-based discretization of the weak form (19) in the context of IGA can be obtained by substituting Eqs. (16) and (17) into Eqs. (19). For the contribution of the residual force vector, i.e. the unbalance of internal and external forces, for an element ranging from $s = s_1$ to $s = s_2$, we have the following expression [49,51,53]:

$$G^{h\,e}_{\text{stat}} = \int_{s_1}^{s_2} \begin{bmatrix} J_{s\xi}^{-1} R'_{i,p} \boldsymbol{I} & R_{i,p} \boldsymbol{R}_i [\boldsymbol{r}']_\times \\ \boldsymbol{0} & J_{s\xi}^{-1} R'_{i,p} \boldsymbol{R}_i \end{bmatrix}^{\mathrm{T}} \begin{bmatrix} \boldsymbol{n}_{\text{int}} \\ \boldsymbol{m}_{\text{int}} \end{bmatrix} ds - \int_{s_1}^{s_2} \begin{bmatrix} R_{i,p} \boldsymbol{I} & \boldsymbol{0} \\ \boldsymbol{0} & R_{i,p} \boldsymbol{I} \end{bmatrix} \begin{bmatrix} \boldsymbol{n}_{\text{ext}} \\ \boldsymbol{m}_{\text{ext}} \end{bmatrix} ds. \tag{22}$$

Here, $[\boldsymbol{r}']_\times$ represent the skew-symmetric matrix, whose axial vector is $\boldsymbol{r}'$, and $\boldsymbol{I} = \text{diag}[1, 1, 1]$. To compute the residual force vector in Eq. (22), the typical Gauss-quadrature rule is used for the numerical integration of the elemental forces. However, we use the classical selective reduced integration technique due to the shear-locking issue. It requires fewer quadrature points than the standard rule. Using a more sophisticated and efficient quadrature scheme for computing the force vectors is beyond the scope of the present work. We refer to the different works in Refs. [83–86] for such variationally consistent and efficient choices of the quadrature points in the context of IGA. The quadrature based integration of the first part of Eq. (22), which is referred to as internal forces $\boldsymbol{f}^e_{\text{int}}$ acting on a NURBS element 'e', is given as

$$\boldsymbol{f}^e_{\text{int},i} = \sum_{qp=1}^{n_{qp}} \begin{bmatrix} R'_{i,p} \boldsymbol{I} & J_{s\xi} R_{i,p} \boldsymbol{R}_i [\boldsymbol{r}']_\times \\ \boldsymbol{0} & R'_{i,p} \boldsymbol{R}_i \end{bmatrix}^{\mathrm{T}} J_{qp} w_{qp}, \tag{23}$$

where $\boldsymbol{f}^e_{\text{int},i}$ corresponds to the contribution of ith control point to the internal force vector. Further, J_{qp} denotes the determinant of the Jacobian matrix enabling the mapping to integration space, and w_{qp} is the weight value associated with the 'qp' quadrature point.

For computing the contribution of the elemental tangent stiffness matrix $\boldsymbol{k}^e$, we have the following expression [53]:

$$\boldsymbol{k}^e = -\frac{\partial \boldsymbol{f}_{\text{int}}}{\partial \boldsymbol{\eta}} \tag{24}$$

To compute the elemental mass matrix, we use the consistent mass matrix approach, which reads as:

$$\boldsymbol{M}^e_{ij} = \int_{s_1}^{s_2} R_{i,p} R_{j,p} \boldsymbol{M}_s \, ds, \tag{25}$$

where $\boldsymbol{M}_s$ is referred as the cross-section mass matrix at coordinate s, and is given as $\boldsymbol{M}_s = \text{diag}[\rho_s A, \rho_s A, \rho_s A, \rho_s J, \rho_s I_{yy}, \rho_s I_{zz}]$ in the centerline reference of the rod. Further, to integrate the dynamic equation of the rod's centerline curve, we use the standard Newmark time integration scheme because of its well-established stability characteristic. For the sake of compactness, we do not show it here and refer to the works by Newmark (1959) [87], Simo and Vu-Quoc (1986) [50] and Tasora et al. (2020) [53] for further details.

3.3. Isogeometric/finite-difference IB approach

Immersed boundary method (IBM) serves as a framework enabling exchange between the fluid and solid solvers. In IBM, the fluid phase is treated using the Eulerian description on a fixed, equidistant Cartesian grid, while the immersed structure is described by a cluster of moving points from the Lagrangian viewpoint. It means that IBM does not require the fluid mesh to be dynamically generated such that it conforms to the fluid–structure interface whenever it changes. Thus, it is a suitable choice in terms of computational efficiency for simulating FSI problems, especially those involving highly flexible structures undergoing large deformations/displacements in unsteady flows. Otherwise, handling the computational cost and complexity of the conforming grid generation is a demanding task, such as in boundary-conforming approaches. In addition to this, IBM allows using suitable numerical techniques to efficiently solve the governing equations of fluid and structure parts independently without requiring any major modifications in the overall system equations for solving complex FSI problems. For this, the no-slip/no-penetration boundary condition is satisfied with a satisfactory approximation by applying an additional forcing to the fluid present in the immediate vicinity of the surface of the immersed structure. In the last two decades, due to its simplicity and advantages, numerous efforts have been devoted to developing a variety of immersed boundary approaches. The main focus has been to broaden the application of the IBM framework to complex FSI applications by utilizing sophisticated solid and/or fluid solvers. However, maintaining the computational efficiency and stability of IBM in such applications remains a challenging task.

In this work, we use the direct-forcing IB approach introduced by Uhlmann [44] to transfer the information between the regular Cartesian grid and the Lagrangian points lying on the slender flexible structure. As noted earlier, we utilize the finite-difference method for the Eulerian variables and IGA for the discretization of the structure. It is known that the IGA technique is capable of accurately capturing the deformation behavior of flexible structures, even at a coarse mesh. However, the long-standing limitation of the IBM framework that the nodal density of the Lagrangian grid must be relatively fine compared to the background Eulerian grid for the satisfactory imposition of the boundary conditions at the interface negates the advantages of the IGA. This is because unnecessary usage of an excessively dense structural mesh can significantly reduce the computational efficiency of the FSI simulations, particularly when many structures are involved. Thus, this work presents a novel IB treatment procedure that enables the usage of a coarse structural mesh at a fixed background Eulerian grid in a finite-difference/isogeometric fluid–structure system. The proposed approach dynamically generates additional Lagrangian marker points with a uniform distribution over a given structural mesh. We fulfill the relative nodal density requirement of the IBM framework by setting the spacing between the Lagrangian markers comparable to the background Eulerian grid. With this, execution of all the IBM operations, i.e. interpolation of the velocity and spreading of the forces, occurs only between the dynamically generated Lagrangian markers and the Eulerian grid. Hence, the resolution of the structural mesh becomes independent of the background Eulerian grid.

The basic steps of the modified IB treatment procedure consisting of the dynamic generation of the Lagrangian marker point over an arbitrarily chosen structural mesh within the isogeometric/finite difference setting for each RK3 sub-step r are summarized in the following:

First, the smallest cell spacing of the Eulerian grid from the three different Cartesian directions, i.e. Δh is retrieved. Using Δh, a Cartesian grid of the parametric coordinates ξ_l is uniformly generated in the NURBS parametric space of the slender structure. Before generating the parametric points over a given structural mesh, the spacing between them is scaled by a predefined value $\Delta\xi_l/\Delta h$ to circumvent the porous representation of the slender structure when it is subjected to large deformations in terms of body force condition. This part of the first step is done only once at the beginning of the simulation, as the stencils related to the Eulerian grid and NURBS parametric points remain the same over time. Thereafter, a uniform distribution of the Lagrangian markers is obtained through the spline interpolations over the physical space of the slender structure with ξ_l. In this, the coordinate vector of each Lagrangian marker $\boldsymbol{x}_l^r$ at the current RK3 sub-step r is computed via the spline interpolation of the control points at the previous time level $\boldsymbol{x}_i^{r-1}$ given by

$$\boldsymbol{x}_l^r(\xi_l) = \sum_{i=1}^{p+1} R_{i,p}(\xi_l)\, \boldsymbol{x}_i^{r-1}\,, \tag{26}$$

where $R_{i,p}$ is the p-order spline function having local support in space $[\xi_i, \xi_{i+p+1}]$. A schematic illustration of the above-described generation procedure of the Lagrangian markers is provided in Fig. 3. For the sake of clarity, the distribution of the Lagrangian markers over the structural mesh of two NURBS elements constructed with the quadratic NURBS functions is depicted. In an analogous fashion, the velocity of the slender structure, obtained via solving Eq. (19), is computed at these new marker points through the splines interpolations:

$$\boldsymbol{w}_l^r(\xi_l) = \sum_{i=1}^{p+1} R_{i,p}(\xi_l)\, \boldsymbol{w}_i^{r-1}\,. \tag{27}$$

Here, $\boldsymbol{w}_i^{r-1}$ denotes the velocity of the ith control point of the structural mesh.

In the second IBM step, the predicted fluid velocity, which is obtained via solving Eq. (11a) is *interpolated* from the nearest neighboring cells to a Lagrangian marker using

$$\tilde{\boldsymbol{u}}(\boldsymbol{x}_l^r) = \sum_{i=1}^{n_x}\sum_{j=1}^{n_y}\sum_{k=1}^{n_k} \tilde{\boldsymbol{u}}(\boldsymbol{x}_{ijk}^r)\, \delta_d(\boldsymbol{x}_{ijk}^r - \boldsymbol{x}_l^r)\, \Delta V\,. \tag{28}$$

where ΔV represents the volume of an Eulerian grid cell. Since we employ a uniform Eulerian grid in all three Cartesian directions, $\Delta V = \Delta h^3$ with Δh as the Eulerian cell spacing. In the present work, we use the regularized Dirac delta function δ_d of Roma

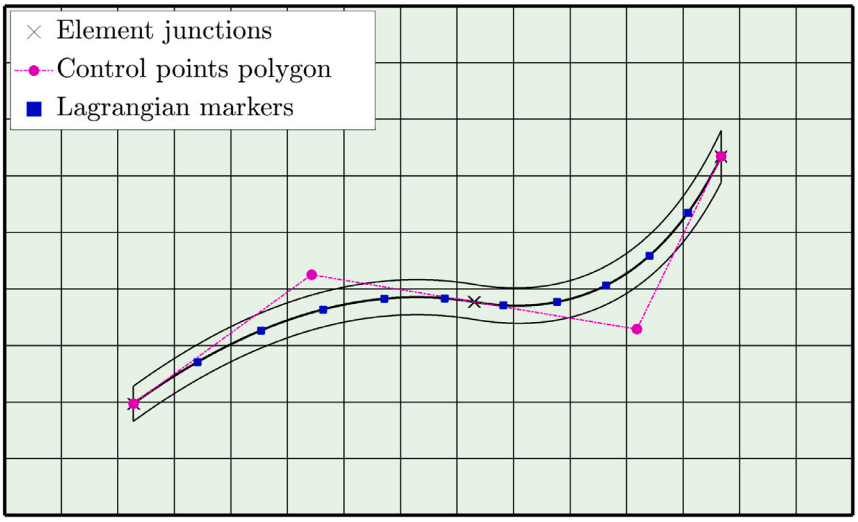

Fig. 3. Schematic of the Lagrangian markers generated over an arbitrarily chosen structural mesh (with $n_{el} = 2$) for a given Eulerian grid. The mesh is discretized with $p = 2$ order of NURBS elements, and its junction points are represented by $\times$. The associated control points and their polygon are shown using the filled circles connected with a line. The spacing between the Lagrangian markers uniformly distributed over the structural mesh is comparable to the background Eulerian grid. (For interpretation of the references to colour in this figure legend, the reader is referred to the web version of this article.)

et al. (1999) [88] for the interpolation of the fluid velocity from the Eulerian grid to each Lagrangian marker due to its good balance between the numerical efficiency and smoothness properties [31,89,90]. It has support over three Eulerian grid cells in each coordinate direction, which ensures the smooth transfer of the information while maintaining the overall numerical efficiency. It is given by the tensor product of one-dimensional functions defined in each direction as [88]

$$\delta_d(\boldsymbol{x}_{ijk} - \boldsymbol{x}_l) = \delta_d(x_{ijk} - x_l)\delta_d(y_{ijk} - y_l)\delta_d(z_{ijk} - z_l) \tag{29}$$

where $\delta_d(x_{ijk} - x_l) = \phi(x_{ijk} - x_l)/h^2$, and the function ϕ defined as

$$\phi(r) = \begin{cases} \frac{1}{6}\left(5 - 3|r| - \sqrt{-3(1-|r|)^2 + 1}\right), & 0.5 \le |r| \le 1.5\,, \\ \frac{1}{3}\left(1 + \sqrt{-3|r|^2 + 1}\right), & |r| < 0.5\,, \\ 0, & \text{otherwise}\,, \end{cases} \tag{30}$$

with $r = (x^r_{ijk} - x^{r-1}_l)/\Delta h$. Fig. 4 illustrates the support domain in the velocity field of the Dirac delta function of Roma et al. [88] at a Lagrangian marker in two dimensions.

In the third IB step, the coupling force located at each Lagrangian marker is then *computed* based on the difference between the velocity of the slender structure and the fluid velocity given by Eq. (28) at the same marker point with

$$\bar{\boldsymbol{f}}(\boldsymbol{x}^r_l) = \frac{\boldsymbol{w}_l(\boldsymbol{x}^r_l) - \tilde{\boldsymbol{u}}(\boldsymbol{x}^r_l)}{\Delta t}\,. \tag{31}$$

In the fourth IB step, the coupling force computed at each Lagrangian marker is distributed to the Eulerian points $\boldsymbol{x}_{ijk}$ of their corresponding support domains with the following *spreading back* operation:

$$\bar{\boldsymbol{f}}(\boldsymbol{x}^r_{ijk}) = \sum_{l=1}^{nl} \bar{\boldsymbol{f}}(\boldsymbol{x}^r_l)\,\delta_d(\boldsymbol{x}^r_{ijk} - \boldsymbol{x}^r_l)\,\Delta V_l\,, \tag{32}$$

where nl denotes the number of Lagrangian markers, and the volume associated with each marker is computed by the product of the cross-section area of the rod A and the Lagrangian marker spacing $\Delta\xi_l$ with $\Delta V_l = A\,\Delta\xi_l$. The coupling forces $\bar{\boldsymbol{f}}(\boldsymbol{x}^r_{ijk})$ arising from Eq. (32) are then included in Eq. (11b) to impose the no-slip condition at the fluid–structure interface. The next sub-steps are to solve the remaining fluid Eqs. (11c)–(11e) to obtain the new velocity $\boldsymbol{u}^r$ and pressure $p^{r+1/2}$ fields.

In the final IB step, the distributed forces and moments at each Lagrangian marker are computed using the coupling force $\bar{\boldsymbol{f}}$ obtained via Eq. (31) with:

$$\begin{aligned} \bar{\boldsymbol{n}}_{\text{ext}}(\boldsymbol{x}^r_l) &= -\rho\,\bar{\boldsymbol{f}}(\boldsymbol{x}^r_l)\Delta V_l\,, \\ \bar{\boldsymbol{m}}_{\text{ext}}(\boldsymbol{x}^r_l) &= -\rho\,\boldsymbol{\zeta} \times \bar{\boldsymbol{f}}(\boldsymbol{x}^r_l)\Delta V_l\,. \end{aligned} \tag{33}$$

The IGA discretized Cosserat rod Eqs. (20)–(21) are then solved to obtain the new position $\boldsymbol{x}^r$, rotation of cross-section $\boldsymbol{q}^r$, translatory velocity $\boldsymbol{w}^r$, and angular velocity $\dot{\boldsymbol{q}}^r$ for the immersed structure.

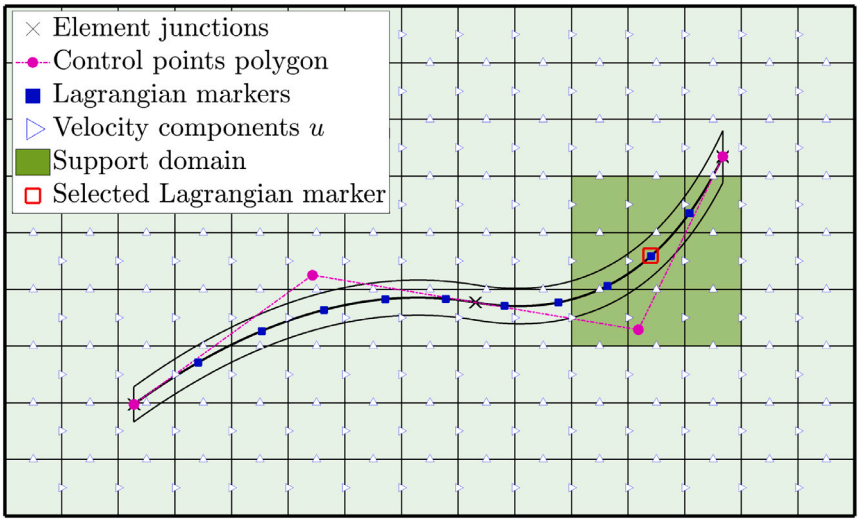

Fig. 4. Schematic of the fluid flow support domain, highlighted in dark green, for a selected Lagrangian marker. The relation between the Lagrangian marker $\boldsymbol{x}_l$ and Eulerian grid $\boldsymbol{x}_{ijk}$ is realized by the regularized Dirac delta function of Roma et al. [88], described above. The staggering of the fluid velocity component in 2D is shown for simplicity. (For interpretation of the references to colour in this figure legend, the reader is referred to the web version of this article.)

The above-mentioned procedure is repeated for each Lagrangian marker at every RK3 sub-step r. The overall algorithm for solving an FSI problem based on the above-described direct forcing IB procedure for a sub-step r of a time-step $t \in [t_n, t_{n+1}]$ is summarized below:

1. Initialize ξ_l parametric coordinate of Lagrangian marker for a given Eulerian grid.
2. Compute predicted fluid velocity $\tilde{\boldsymbol{u}}$ using Eq. (11a) without accounting for $\tilde{\boldsymbol{f}}$.
3. Compute coordinates of the Lagrangian markers $\boldsymbol{x}_l$ over NURBS mesh via Eq. (26).
4. Interpolate velocity of the structure at each Lagrangian marker $\boldsymbol{w}_l$ using Eq. (27).
5. Interpolate fluid velocity $\tilde{\boldsymbol{u}}$ to each Lagrangian marker $\tilde{\boldsymbol{u}}(\boldsymbol{x}_l^r)$ via Eq. (28).
6. Compute coupling force at each Lagrangian marker $\bar{\boldsymbol{f}}(\boldsymbol{x}_l^r)$ using Eq. (31).
7. Spread back $\bar{\boldsymbol{f}}(\boldsymbol{x}_l^r)$ over Eulerian support domain of each marker using Eq. (32).
8. Compute distributed force $\bar{\boldsymbol{n}}_{\text{ext}}(\boldsymbol{x}_l^r)$ and moment $\bar{\boldsymbol{n}}_{\text{ext}}(\boldsymbol{x}_l^r)$ for structure via Eq. (33).
9. Solve fluid flow Eqs. (11b)–(11e) updated with $\bar{\boldsymbol{f}}(\boldsymbol{x}_{ijk}^r)$ to compute $\boldsymbol{u}^r$ and $p^{r+1/2}$.
10. Solve IGA Cosserat rod Eqs. (20)–(21) to compute: $\boldsymbol{x}$, $\boldsymbol{q}$, $\boldsymbol{w}$, $\dot{\boldsymbol{q}}$, and return to step 2.

With the above-described procedure, the presented isogeometric/finite difference IB approach allows for generating an additional Lagrangian grid together with the flexibility of controlling the marker spacing over a fixed structural mesh. This is a remarkable feature for the FSI simulations involving flexible structures as with this: (1) the density of the structural mesh becomes fully independent of the Eulerian grid density. Hence, a very coarse structural mesh, which is sufficient to capture the elastic responses of the filament undergoing finite deformations, can be used for the solid solver as compared to the standard IB method, which otherwise requires the nodal density of the structural mesh to be nearly the same as the Eulerian grid. (2) A suitable Lagrangian marker grid, which is comparatively fine to the background Eulerian grid, can be easily generated at a coarse structural mesh without losing the accuracy of the enforcement condition at the interface. In Section 5, we will demonstrate the performance of the proposed IB approach. As compared to the standard IB method, it considerably reduces the computational efforts associated with the solid solver of the finite-difference/isogeometric FSI framework without the loss of numerical stability and robustness.

In Section 5, we also show that increasing the relative Lagrangian marker spacing $\Delta\xi_l/\Delta h$ beyond a specific value increases the error on the no-slip/no-penetration condition at the interface. Thus, a result of lower accuracy is obtained. On the other hand, on reducing $\Delta\xi_l/\Delta h$ below a specific value does not improve the interface resolution, and thus, nearly identical results are obtained.

4. Solid solver validations

In this section, we present validations of our solid solver, i.e. IGA-based implementation of the geometrically exact isogeometric Cosserat rod, for the static and dynamic cases involving large deformations of the flexible beam.

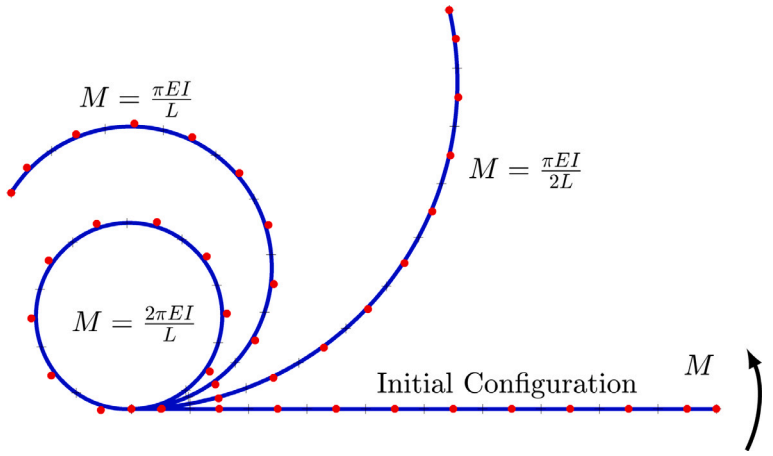

Fig. 5. Bending of a straight cantilever subjected to the moment M applied at its free end: Initial and deformed configuration of the centerline for different load values. The beam is discretized using 10 quadratic order NURBS elements. (For interpretation of the references to colour in this figure legend, the reader is referred to the web version of this article.)

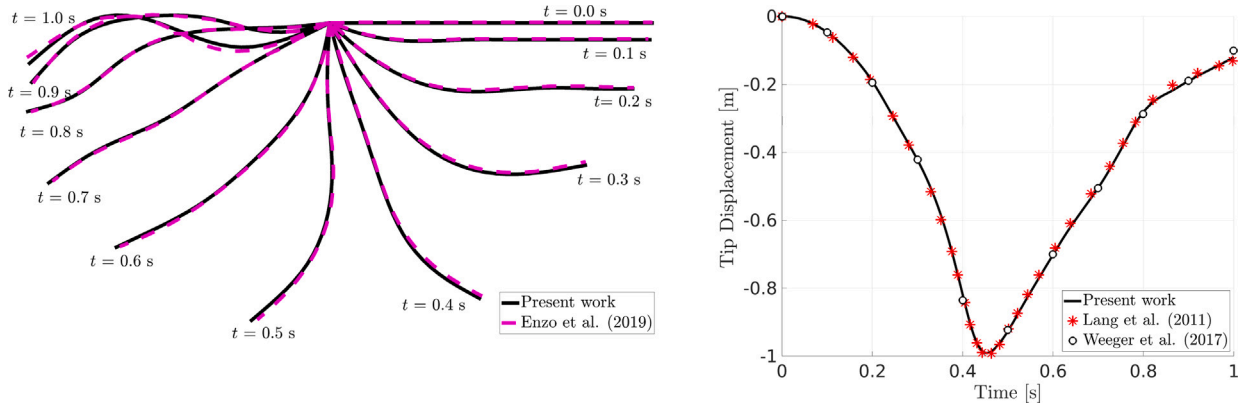

Fig. 6. Top: Comparison of the different configurations of a flexible rod swinging under gravity from time 0 to 1 with a time interval 0.1. Bottom: Comparison of the vertical tip displacement of the rod with the results from the literature. The rod is discretized using 30 quartic order of NURBS elements. (For interpretation of the references to colour in this figure legend, the reader is referred to the web version of this article.)

4.1. Bending of a straight cantilever

In the first numerical example, we test the validity of our solid solver with one of the most occurring benchmarks in literature, which is used for nonlinear beam formulations. It involves the pure bending of an initially straight cantilever beam of length L by a concentrated moment M at the tip of its free end. The setup of the problem is shown in Fig. 5. The analytical solution to this problem is a circle with a radius EI/m. The moment required to bend the beam in the shape of a perfect circle $m = 2\pi EI/L$ [49]. Here, the beam is of unit length and discretized with ten second-order NURBS elements, denoted by N_2. Due to the large deformations, we carry out the nonlinear static analysis by gradually increasing the torque value in 20 steps. The deformed configurations of the beam for different values of end moment values are shown in Fig. 5. It can be observed that the final configuration of the beam obtained with our solid solver is in excellent agreement with the analytical solution.

4.2. Swinging of a flexible rod under gravity

As compared to the first numerical example, where we used a very stiff beam, here we consider a rod of high flexibility having a circular-cross section with diameter $d = 0.01$ m and length $L = 1.0$ m. Initially, at time $t = 0.0$ it is placed horizontally with its left end pinned as shown in Fig. 6. The Young's modulus, Poisson's ratio, and material density are $E = 5 \times 10^6$ N/m^2, $\nu = 0.5$, and $\rho_s = 1100$ kg/m^3. We discretize the rod with 30 quartic order NURBS elements, i.e. N_4. The overall simulation swinging time is 1.0 s with a time-step size $\Delta t = 5 \times 10^{-3}$ s. Fig. 6(a) shows the various configurations of the centerline of the rod from time $t = 0.0$ to $t = 1.0$ s with a time interval of 0.1 s.

For comparison, we use the results from Enzo et al. [62]. As can be seen, the different configurations of the rod are in agreement with those reported in [62]. Further, the comparison of the time history of the vertical displacement of the tip obtained from the present work with that reported in the Refs. [71,91] is provided in Fig. 6(b). Again, the result obtained with our solid solver is in excellent agreement with those in the literature.

5. FSI benchmarks and results

Since the fluid solver utilized in the present work has been extensively validated for different flows [78,79], we present the validation and performance of our isogeometric/finite-difference framework using two different FSI benchmarks involving slender flexible structures. We systematically vary the mesh resolution of the immersed structure at a fixed background Eulerian grid to demonstrate the efficacy of our isogeometric/finite-difference FSI framework. In each case, the relative spacing between the Lagrangian markers over a structural mesh and the Eulerian grid is kept comparable. The minimum relative grid spacing below which the results can be considered independent is also identified.

5.1. Flapping of a flexible filament in a uniform flow

In this numerical example, we consider the flapping motion of a flexible filament in a uniform flow to demonstrate the capabilities of the developed computational framework. This example was first studied by Zhang et al. [3] and has been extensively used to study the performance of various FSI schemes in capturing the dynamics of a flexible structure in the fluid [35,48,92–94]. It serves as a model to replicate the flag-flapping phenomenon in the wind, locomotion of swimmers and micro-organisms, and investigate the filament motion in the soap film.

5.1.1. Description and validation

The problem setup, taken from Huang et al. [95], is shown in Fig. 7. A flexible filament of length $L = 1.0$ is hinged at the origin in the computational domain with dimensions $[-2L, 6L] \times [-4L, 4L]$ along the x- and y-directions. As shown in Fig. 7, the filament is initially inclined at an angle $\theta = 0.1\pi$ w.r.t. the x-axis. The boundary conditions used for the fluid problem are: inlet and outlet along the horizontal boundaries and free-shear walls along the vertical boundaries. The directions of the flow and the gravity force are along the x-axis. Based on the incoming flow velocity U, filament length L, and fluid kinematic viscosity ν, the Reynolds number at which the simulations are performed is $Re = 200$. The other parameters are: Froude number $\mathrm{F} = U/\sqrt{gL} = 1.414$, and the solid to fluid density ratio $\rho_r = \rho_s/\rho = 150$. Unlike in [95], where an inextensibility constraint is imposed on a fiber by solving an additional equation, in the present work, we use a large value of the (non-dimensional) axial stiffness coefficient, i.e. $K_A = Ed/(\rho U^2 L) = 2500$ as in [48], to approximately satisfy the inextensibility condition. The bending stiffness of the filaments is the same as in [95], i.e. $K_B = EI/(\rho U^2 L^3) = 0.0015$.

First, we validate the implementation of our FSI framework against the result presented in [95]. For this, we use the same number of points for the Eulerian and Lagrangian grids as in [95]. Specifically, we use 528×528 number of elements along the x- and y-directions, yielding a uniform Eulerian grid with spacing $\Delta h = 0.0152$. For the discretization of the filament, we employ standard $n_{\mathrm{el}} = 64$ number of linear-order NURBS elements, denoted by N_1. With this, the spacing of the Lagrangian points is nearly equal to that of Eulerian grid points, i.e. $G_{\mathrm{r}} = \Delta x_l/\Delta h \approx 1$.

Fig. 8 illustrates the time evolution of the transverse displacement of the trailing edge of the filament. It can be seen that the result obtained with the standard N_1 discretization of the filament with $G_{\mathrm{r}} = 1$ is in good agreement with the numerical result of

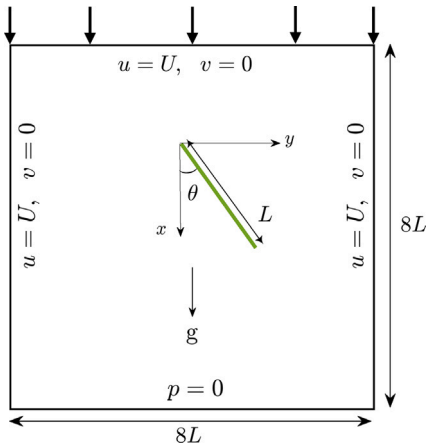

Fig. 7. Schematics of the computational domain and boundary conditions for FSI simulation of a flexible filament in uniform flow. (For interpretation of the references to colour in this figure legend, the reader is referred to the web version of this article.)

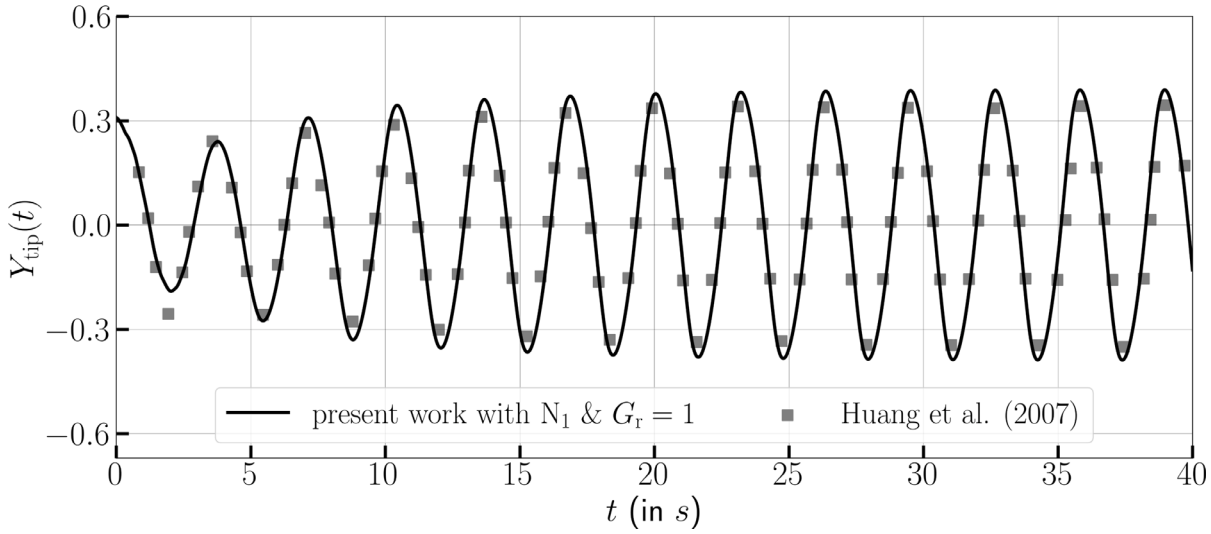

Fig. 8. Comparison of the time evolution of the trailing edge transverse displacement of the filament in a uniform stream.

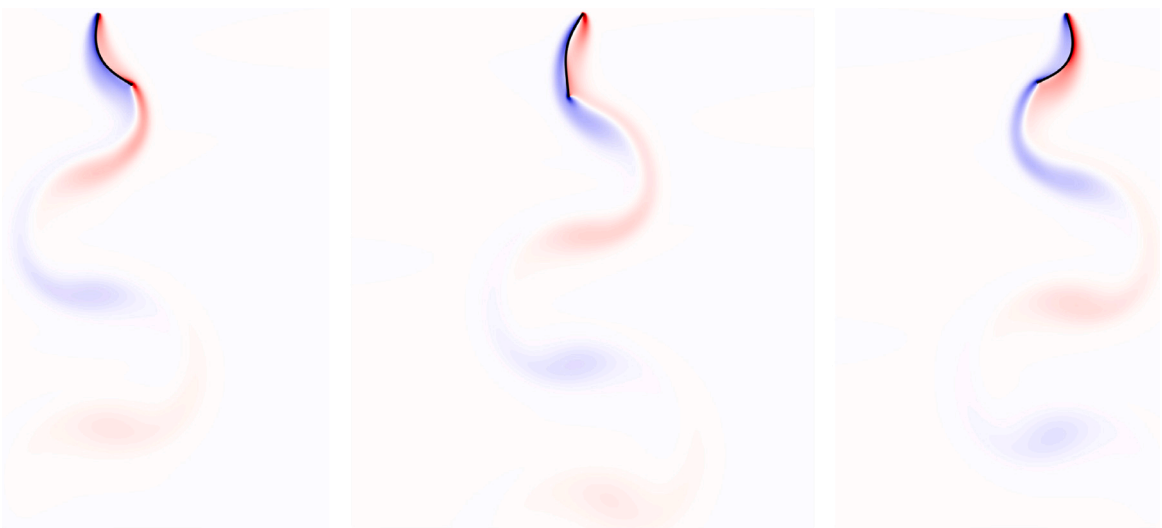

Fig. 9. Instantaneous vorticity contours of the flow around the centerline of the filament at time: (a) $t = 20$, (b) $t = 20.85$, and (c) $t = 21.7$ s. (For interpretation of the references to colour in this figure legend, the reader is referred to the web version of this article.)

Huang et al. [95]. The filament undergoes seven transient oscillations before attaining the self-sustaining periodic flapping state. The instantaneous stream-wise vorticity contours at three-time instants of a periodic flapping cycle, where the filament goes from maximum positive to minimum negative vertical deflections, are provided in Fig. 9. Further, different filament configurations at various time instants during the periodic flapping cycle are provided in Fig. 10, showing the symmetric behavior of the filament deformation.

5.1.2. Performance analysis

Next, we demonstrate the performance of the developed framework constituting the isogeometric/finite-difference immersed boundary coupling procedure, by systematically coarsening the mesh resolution of the NURBS discretized fiber at a fixed background Eulerian grid. We assess the accuracy of the FSI results at the Lagrangian grid spacings: $G_r \approx 2, 4, 6, 8$ relative to the fixed 528×528 Eulerian grid. These spacings are corresponding to $n_{el} = 32, 16, 11, 8$ number of N_2 based structural elements. The mesh resolutions for the fiber at a fixed background grid corresponding to different G_r are illustrated in Fig. 11. In all cases, a uniform Lagrangian

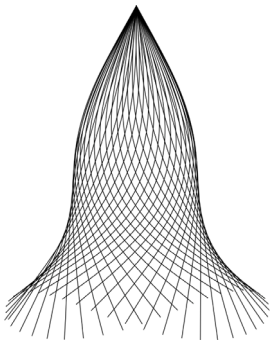

Fig. 10. Snapshots of the various configurations of the filament in uniform flow at several time instants during the periodic flapping.

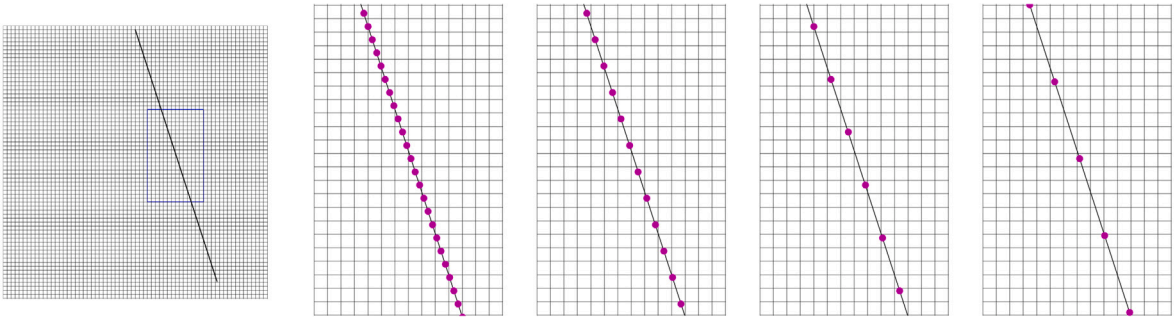

(a) Selected domain for enlarged view (b) $G_r = 1$ (c) $G_r = 2$ (d) $G_r = 4$ (e) $G_r = 6$

Fig. 11. Illustration of the mesh resolution used for the centerline of the fiber at a (subset of) fixed background grid for different grid spacing ratio G_r. (For interpretation of the references to colour in this figure legend, the reader is referred to the web version of this article.)

marker spacing close to 0.7 of the Eulerian grid spacing Δh is taken to avoid any flow leakage [31,64]. In order to reduce the complexity of this study, we fix the interpolation order of the NURBS basis function to second-order, i.e. N_2 in the following. Such a NURBS based discretized ensures the necessary C^1-continuity across the internal points of the filament. The other simulation parameters are the same as described in the previous sub-section. Fig. 12 shows the results at different resolutions, where the result with the standard $G_r = 1$ description is used as reference. Two observations are made: (i) the proposed method provides consistent results with different G_r except $G_r = 8$. (ii) $G_r = 6$, which is the coarsest Lagrangian mesh, yields nearly the same accurate result at the fixed Eulerian grid spacing as compared to the standard $G_r = 1$ based description. Note that $G_r = 6$ requires nearly 82% lower number of DOFs as compared to standard $G_r = 1$ based description and, thus, considerably reduces the overall simulation cost, see Table 1. Although with $G_r = 8$, the amplitude of the flapping motion of filament is similar to that of $G_r = 1$, the phase of the result shifts slightly. Such a non-physical shift is due to using a too-coarse resolution to capture the dynamics of the filament.

Since in the proposed isogeometric/immersed boundary coupling procedure, the spacing of the Lagrangian markers can be set independently of the Lagrangian mesh of the filament, we investigate the impact of the marker spacing on the accuracy of the FSI results at a fixed Lagrangian mesh. Fig. 13 shows the result with the coarsest Lagrangian mesh, i.e. $G_r = 6$ at two different relative spacings of the Lagrangian markers. Note that the Eulerian grid is fixed as above. It can be seen the usage of marker spacing $\Delta\xi_l/\Delta h = 1.1$ leads to a loss of accuracy as compared to $\Delta\xi_l/\Delta h = 0.7$. This is because the increase in the relative marker spacing beyond a specific value reduces the accuracy of the no-slip/no-penetration condition at the interface and yields less accurate FSI results, see also e.g. [31,90]. On the other hand, the further reduction of $\Delta\xi_l/\Delta h$ beyond a specific value does not affect the interface resolution at a fixed Lagrangian mesh and identical results are obtained (not shown here).

5.1.3. Convergence study

In this section, we further use the results from the flapping of a flexible filament in a uniform flow to demonstrate the convergence behavior of the developed computational framework. To this end, we employ six uniform Eulerian grids: 156×156, 234×234, 352×352, 528×528, 792×792, and 1188×1188 with a constant refinement ratio of 1.5. The Lagrangian meshes having relative grid spacings $G_r = 1, 2, 4, 6$ w.r.t. to these six uniform Eulerian grids are utilized. For each G_r, the h-refinement on the uniform knot vector is performed while keeping the refinement ratio fixed to 1.5. Table 1 provides the summary of the Eulerian, and Lagrangian meshes at different G_r along with the spacings of each grid/mesh. With the aim of analyzing the overall numerical accuracy in space and time simultaneously, the time-step for each grid is taken such that the ratio between the Eulerian grid spacing and time-step

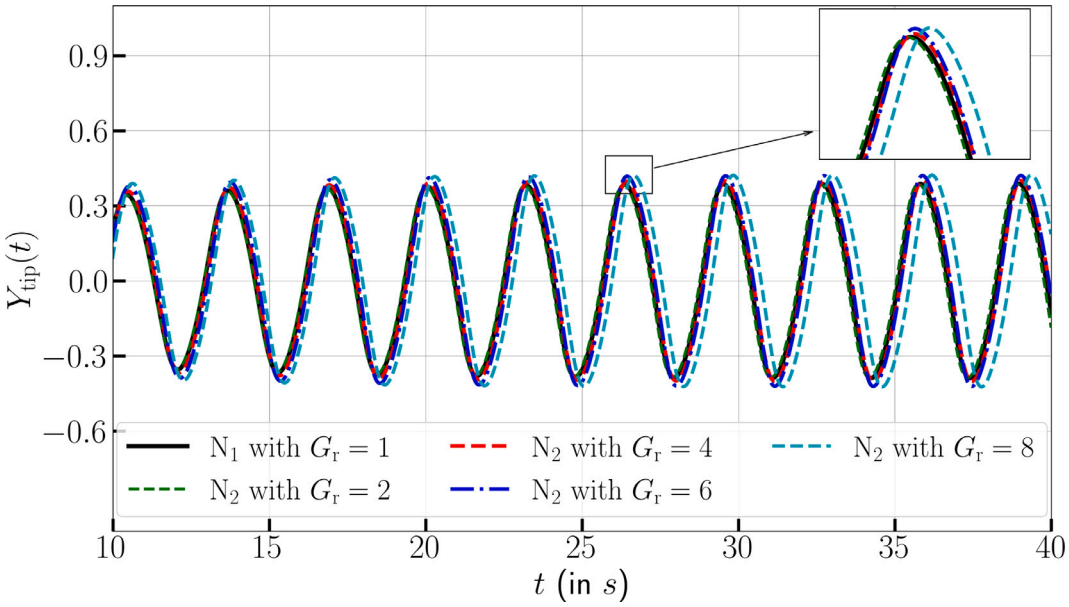

Fig. 12. Time traces of trailing edge transverse locations of the filament in a uniform stream with different relative grid spacings G_r at a fixed Eulerian grid. (For interpretation of the references to colour in this figure legend, the reader is referred to the web version of this article.)

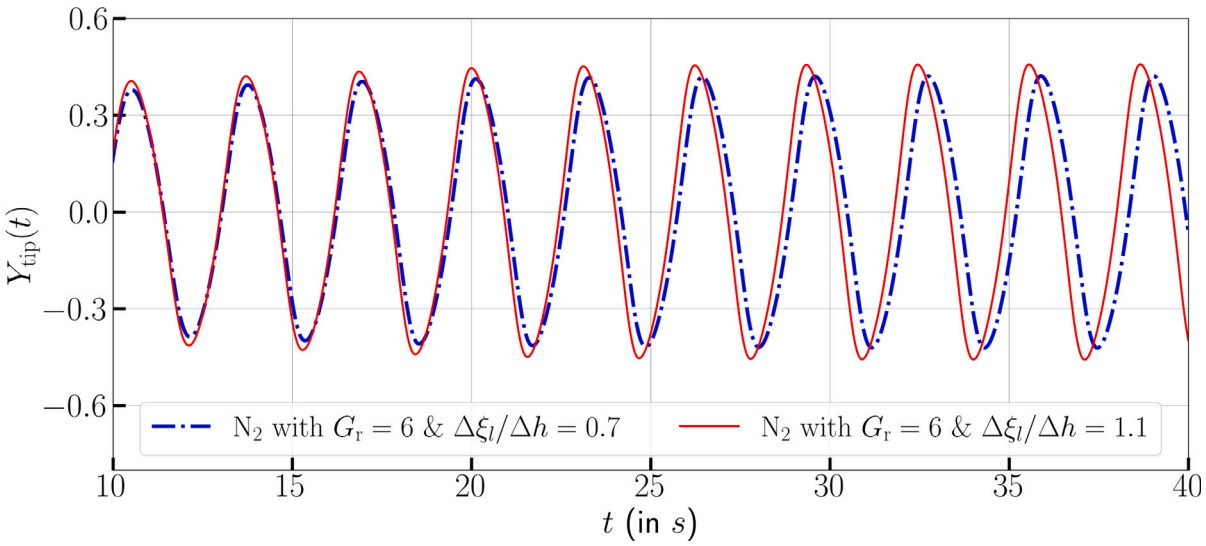

Fig. 13. Comparison of the time traces of the trailing edge transverse location of the filament in a uniform stream with different values of Lagrangian marker spacings at a fixed Eulerian as well as Lagrangian mesh. (For interpretation of the references to colour in this figure legend, the reader is referred to the web version of this article.)

size remains constant, i.e. $\Delta h/\Delta t = 8U$. This means that the CFL (Courant–Friedlich–Lewy) number based on the inflow velocity is the same for all grids. To assess the convergence behavior, two error measures are defined: $\epsilon(A)$ for the flapping amplitude and $\epsilon(T)$ for the oscillation period of the flapping state. Each error is evaluated using

$$\epsilon(\square) = \frac{|\square - \square^{\text{ref}}|}{\square^{\text{ref}}} \tag{34}$$

where $\square^{\text{ref}}$ is the value of a selected variable at the finest 1188×1188 Eulerian grid used as a reference.

The convergence of $\epsilon(A)$ and $\epsilon(T)$ against grid refinement are reported in Fig. 14. From these, mainly two observations are made: (i) With the proposed FSI procedure, a consistent second-order convergence rate on the finer grids is achieved. It is therefore demonstrated that the proposed FSI procedure's overall accuracy ensures the fundamental solvers' accuracy order. (ii) For different values of G_r, nearly identical accuracy at a fixed mesh level is attained. This implies that the method enables the use of much

Table 1
Summary of the computational setting for the Eulerian grid and Lagrangian meshes at different G_r for the convergence study.

m_i	Eulerian		$G_r = 1$		$G_r = 2$		$G_r = 4$		$G_r = 6$	
	Grid	Δh	n_{el}	Δx_l	n_{el}	Δx_l	n_{el}	Δx_l	n_{el}	Δx_l
m_1	156 × 156	0.0513	19	0.0526	9	0.1111	4	0.2500	3	0.3333
m_2	234 × 234	0.0342	28	0.0357	14	0.0714	7	0.1429	5	0.2
m_3	352 × 352	0.0227	42	0.0238	21	0.0476	11	0.0909	7	0.1429
m_4	528 × 528	0.0152	64	0.0156	32	0.0312	16	0.0625	11	0.0909
m_5	792 × 792	0.0101	99	0.0101	48	0.0208	24	0.0417	17	0.0588
m_6	1188 × 1188	0.0067	148	0.0068	72	0.0139	36	0.0278	25	0.04

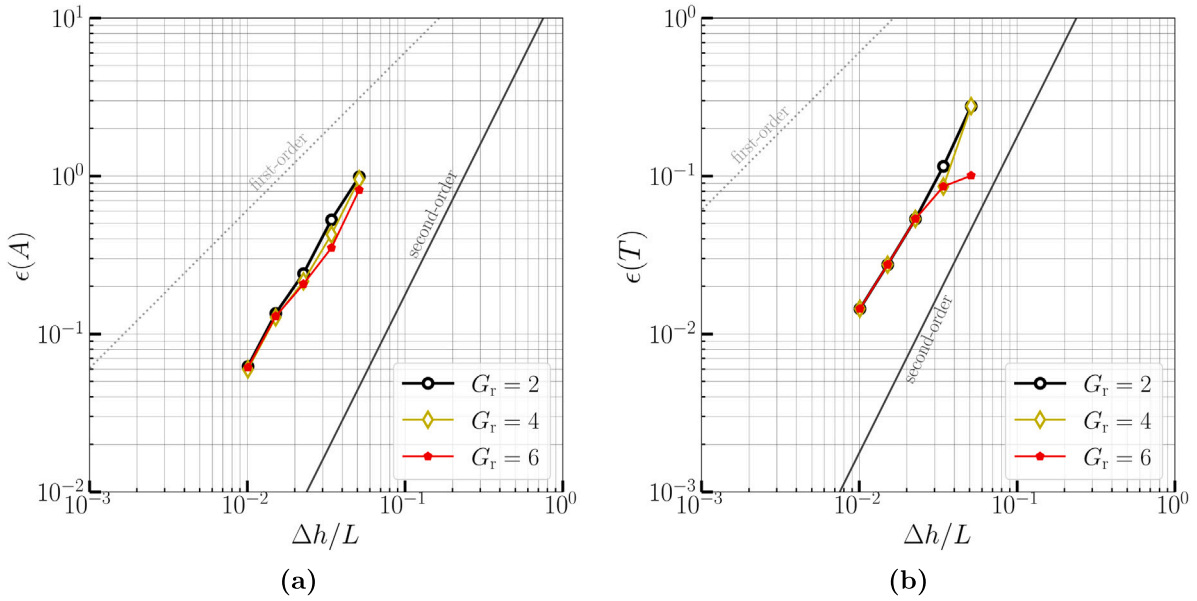

Fig. 14. Relative error versus grid resolution in terms of: (a) amplitude and (b) period of the flapping cycle of the flexible filament in a uniform stream. (For interpretation of the references to colour in this figure legend, the reader is referred to the web version of this article.)

coarser structural meshes for a given Eulerian grid compared to the standard approach without any noticeable loss of accuracy. Furthermore, the method verifies itself to be robust, yielding nearly identical error values with different G_r. In addition, a closer look at the figure reveals some degree of phase shift in the convergence of $\epsilon(A)$ and $\epsilon(T)$ at the initial two mesh levels, particularly noticeable when employing $G_r = 6$. This shift is attributed to using an overly coarse mesh resolution, denoted as m_1, for the fiber, which is unable to accurately capture the dynamics of the flapping filament, especially the oscillation period. This is similar to the observation made for the $G_r = 8$ at mesh level m_4 in Fig. 12. A further closer look at Fig. 14 reveals that as the mesh resolution of the fiber is further increased, i.e. m_2 to m_6, the error in the phase of the convergence diminishes and finally disappears. Notably, $G_r = 6$ yields an accuracy level nearly identical to the accuracy achieved with other G_r based descriptions. For completeness, time histories of the filament tip positions for $G_r = 6$ are illustrated in Fig. 15 w.r.t. the reference solution.

5.2. Flexible filaments in oscillatory flow

We use this example for the following two reasons. First, to test the validity of our FSI framework against the results from experiments and computations by Pinelli et al. [96]. Second, to demonstrate the capabilities of the proposed isogeometric/immersed boundary approach to simulate a row of slender structures in a viscous flow in three dimensions. This example concerns 5 flexible filaments clamped vertically at the centerline of the bottom wall of a three-dimensional rectangular channel subjected to a pulsating flow.

5.2.1. Description and validation

A schematics of the computational setup, taken from Pinelli et al. [96], is illustrated in Fig. 16. The computational domain has dimensions: $L_x \times L_y \times L_z = 10L \times 6L \times 5L$ along the streamwise, wall-normal, and spanwise directions, and is discretized with 160 × 96 × 80 Eulerian grid points. The following boundary conditions are used: no-slip along the wall-normal y-direction and periodic along the x- and z-directions. In the experiment, the channel is filled with glycerin having kinematic viscosity $\nu = 1$ cm^2 s^{-1} and subjected to an oscillating pressure gradient. Based on the maximum flow velocity in the channel, i.e. $u_{max} = 60$ cm/s, the

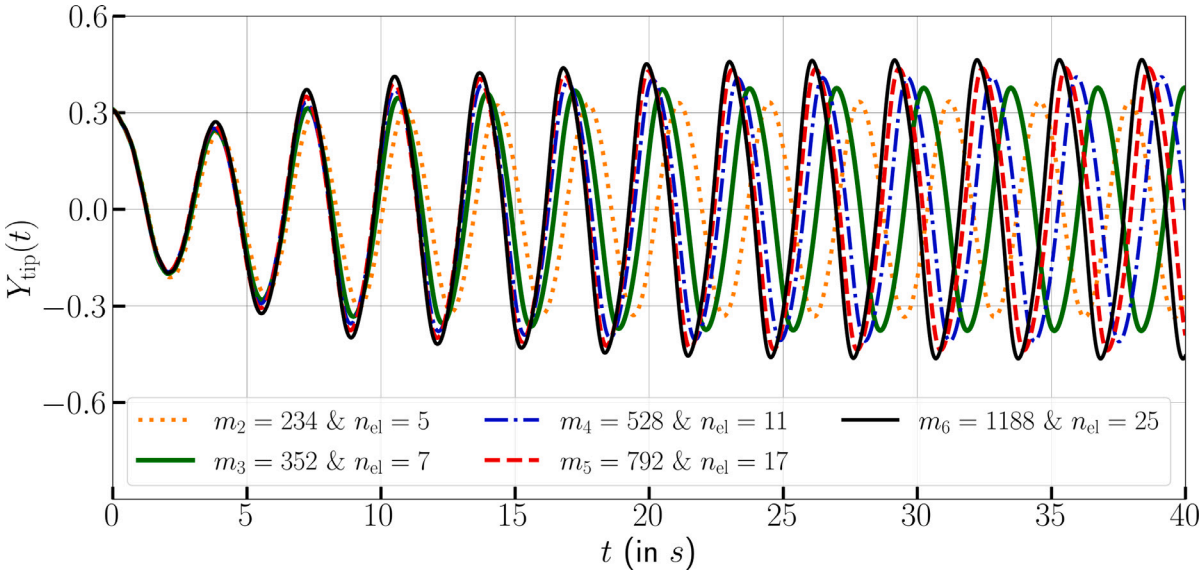

Fig. 15. Time traces of the trailing edge transverse location of the flexible filament in a uniform flow case at different Lagrangian and Eulerian grid resolutions. The relative spacing between the Lagrangian mesh and the Eulerian grid is $G_{\text{r}} = 6$. The black curve with the finest mesh m_6 is a reference solution. (For interpretation of the references to colour in this figure legend, the reader is referred to the web version of this article.)

bulk Reynolds number is: $Re = u_{\max} L/\nu = 60$. The length of each cylindrical filament is $L = 10$ mm, and the diameter is $D = 1$ mm. The separation distance between the filaments is half the filament length. The pulsating frequency of the channel is set to 1 Hz, which matches the natural frequency of the filaments (having Young modulus $E = 1.23$ MPa). For the discretization of each filament, 16 number of linear order NURBS elements N_1 are used as in [96]. With this, the Lagrangian to Eulerian grid spacing ratio is $G_{\text{r}} = 1$.

Fig. 17 shows instantaneous snapshots of the vorticity in the oscillating channel flow. The quantitative comparisons are provided in Fig. 18, showing the time traces of the tip displacement of the last filament. As seen, the frequency of the oscillations and amplitude of the displacement obtained with the present work matches the experimental and numerical results of Pinelli et al. [96]. The small difference in the amplitude between the present work and the numerical result of Pinelli et al. [96] could be due to using different beam models for the filament. Pinelli et al. [96] used the Euler–Bernoulli beam model, while the Cosserat rod model is used in the present work.

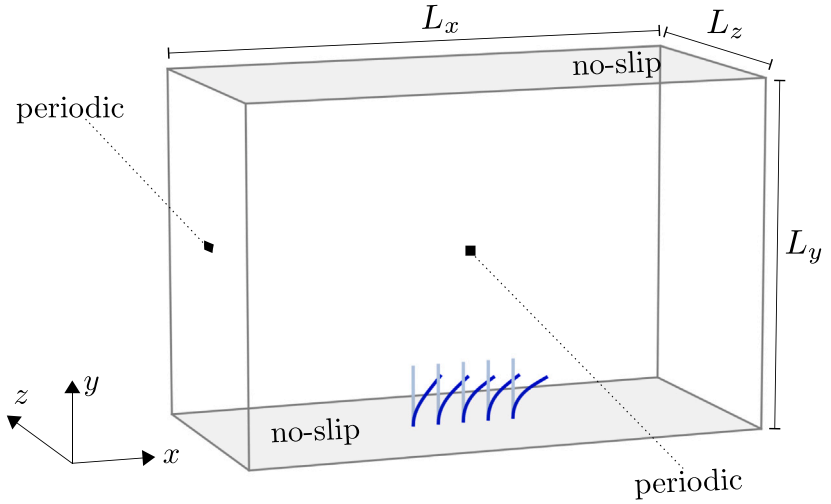

Fig. 16. Schematic illustration of the computational domain for FSI simulation of a row of filaments in oscillatory flow. The maximum deformed configuration of the filaments (in blue) w.r.t. their initial configurations (in sky blue). (For interpretation of the references to colour in this figure legend, the reader is referred to the web version of this article.)

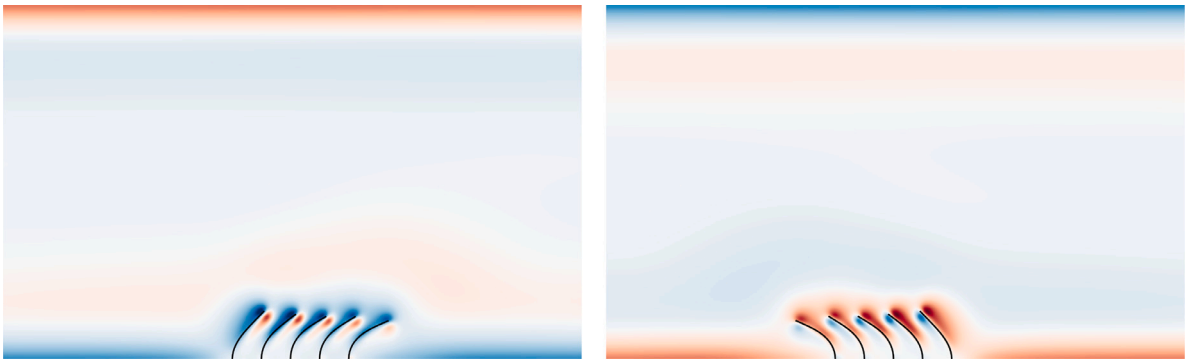

Fig. 17. 2D color contours of the instantaneous spanwise vorticity in the wall-normal plane where filaments are clamped. The positions of the flexible filaments centerline are shown at the time of maximum positive (left) and negative deflections (right). (For interpretation of the references to colour in this figure legend, the reader is referred to the web version of this article.)

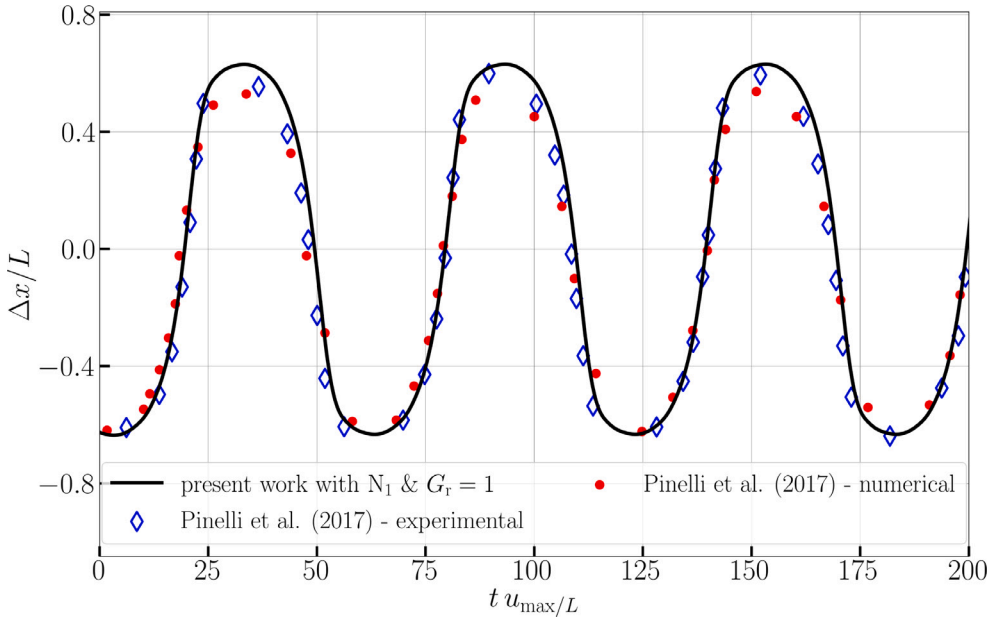

Fig. 18. Comparison of the time evolution of the streamwise tip displacement of the last filament in an oscillatory channel flow. (For interpretation of the references to colour in this figure legend, the reader is referred to the web version of this article.)

5.2.2. Performance investigations

Fig. 20 shows the performance of the proposed finite-difference/isogeometric IB approach for different relative Lagrangian and Eulerian grid spacings. The spacing of the Eulerian grid 0.0625 is kept fixed as described above, while each filament is discretized with N_2 based $n_{el} = 8, 4, 3, 2$ elements, resulting in $G_r \approx 2, 4, 6, 8$. The mesh resolutions of the fiber at a fixed background grid obtained with different G_r are illustrated in Fig. 19. Further, for all cases, the ratio of the Lagrangian marker spacing to the Eulerian grid spacing is kept close to 0.7 as in the first FSI example. From Fig. 20, two main observations are made: (i) The proposed IB approach provides consistent results in terms of frequency of oscillation and displacement amplitude with different G_r, except $G_r = 8$. Thus, demonstrating the versatility of the approach for more than one filament. (ii) $G_r = 6$ is the coarsest Lagrangian mesh, providing identical results as compared to the standard $G_r = 1$ based description. It requires nearly 71% lower number of DOFs compared to $G_r = 1$ for each filament, thereby considerably reducing the computational efforts associated with FSI simulations. Furthermore, taking a closer look at Fig. 20 reveals that the oscillation frequency obtained with $G_r = 8$ is comparable to $G_r = 1$. However, the figure shows a small difference in the amplitude of the displacement oscillations.

5.3. Submerged vegetation in a turbulent channel flow

We consider the flow over submerged vegetation as the final example to demonstrate the capabilities of our computational framework to simulate a large number of highly flexible filaments in a turbulent flow. Considering the great interest in understanding

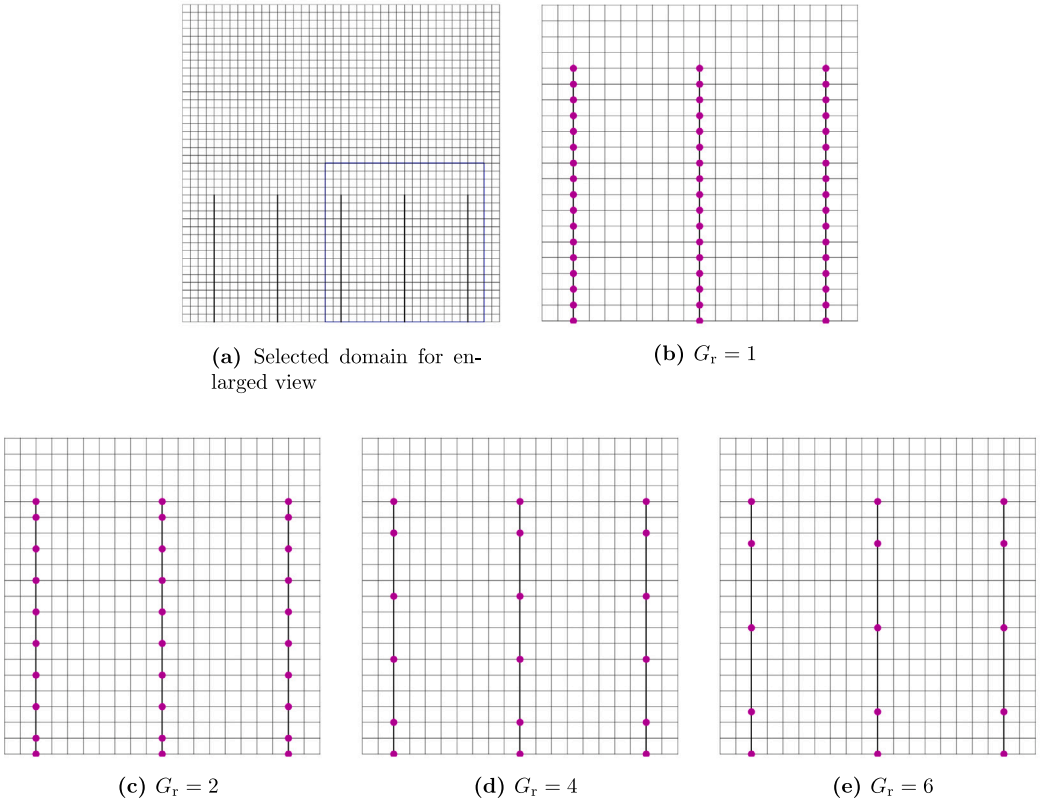

Fig. 19. 2D illustration of the mesh resolutions used for the centerline of the fiber at a (subset of) fixed background grid for different grid spacing ratio G_r.. (For interpretation of the references to colour in this figure legend, the reader is referred to the web version of this article.)

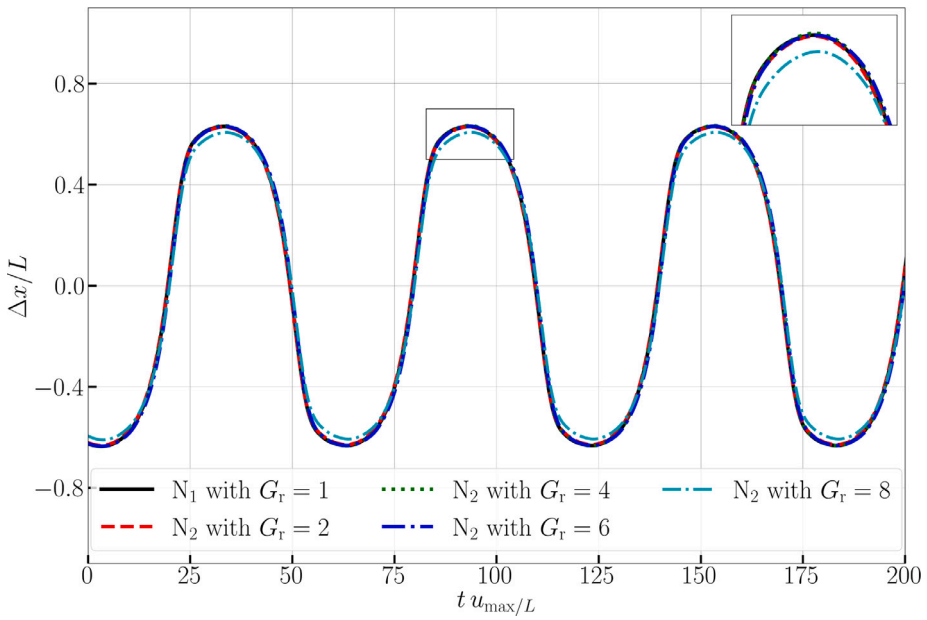

Fig. 20. Time evolution of the streamwise tip displacements of the last filament with different relative grid spacing ratios G_r at a fixed Eulerian grid. (For interpretation of the references to colour in this figure legend, the reader is referred to the web version of this article.)

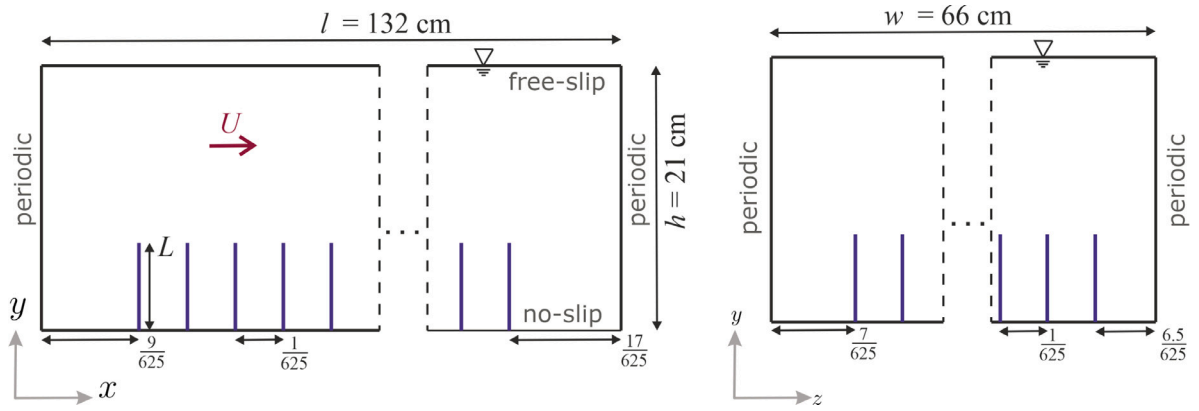

Fig. 21. Schematics of the computational domain and boundary conditions for the submerged vegetation example. (For interpretation of the references to colour in this figure legend, the reader is referred to the web version of this article.)

how fluid mechanics influence the behavior of the submerged vegetation patch and its impact on the ecology of lotic ecosystems, considerable efforts have been dedicated to this problem, cf. Refs. [97,98] for experimental studies, [99,100] for the analytical solutions, and Refs. [65,68,101–104] for numerical analysis of the submerged canopies.

The setup of the problem considered in the present study is depicted in Fig. 21. It involves a patch consisting of 80 × 40 slender flexible filaments submerged within a three-dimensions open channel flow. The computational domain is of size $l \times h \times w = (132, 66, 21)$ cm^3 along the streamwise, spanwise, and wall-normal directions. The no-slip boundary condition is applied to the bottom surface of the channel, while the free-slip boundary condition is taken at its top surface. Periodic boundary conditions are used in the streamwise and spanwise directions. The flow is driven by enforcing a constant bulk velocity $U = 5$ m/s. Based on the bulk velocity U, channel height h, and kinematic viscosity of the fluid, i.e. $\nu = 10^{-3}$ m^2/s, the Reynolds number is $Re_h = 42,000$. Further, the density ratio between the filament and fluid is taken as 10. In the setup, the filaments of length $L = 70$ mm, radius $r_s = 1$ mm, and Young's modulus $E = 10^7$ N/m^2 are clamped at the bottom boundary of the channel with equal spacing of $\frac{1}{625}$ cm in both the streamwise and spanwise channel directions. In the immersed array, the first filament is set at a distance of $\frac{9}{625}$ cm and $\frac{7}{625}$ cm from the left corner of the computational boundary in the x- and z-directions. Consequently, the last filament of the array is at a distance from $\frac{17}{625}$ cm and $\frac{6.5}{625}$ cm in the same directions, as shown in Fig. 21. The computational domain is discretized by $576 \times 288 \times 92$ cells along the streamwise, spanwise, and wall-normal directions. This grid resolution corresponds to one of the cases used for simulating flow through artificial canopy example in [65]. Each fiber is discretized with 30 linear-order N_1 elements, therefore 3200 fibers use 96,000 elements, as per the standard $G_r = 1$ based description. In order to assess the computational performance of the developed framework, we use the $G_r = 6$ based description of the fibers, which requires 6 times lower number of elements as compared to $G_r = 1$.

Fig. 22 shows instantaneous flow and vegetation snapshots at an arbitrary time instance, $t = 32.5$ s from the $G_r = 6$ based description. Fig. 22(a) shows that the flow slows down in the vicinity of the filament patch and that the collective interaction of the flexible filaments leads to the formation of the typical monami-motion of the fluid, as also observed in [65,68,102,103]. The bent configuration of the fibers, colored by their absolute deflection from the initial position and normalized with fiber length, are illustrated in Figs. 22(b) at the same time instance. The corresponding top view of the wavelike configuration of the flexible filament patch is shown in Fig. 22(c).

Given the challenges associated with experimentally capturing the evolution of 3D coherent fluctuation patterns within the fluid field, numerical methods have become the preferred choice for studying the interaction of numerous highly flexible filaments with a turbulent flow. It is important to note that, within the current simulation parameters, there are a few instances where two or a few filaments come into contact with one other. However, the results presented here do not account for a contact model between the filaments. In the current example, the deflection of the filaments is solely driven by the hydrodynamic forces arising from the interactions with the surrounding fluid flow. We utilize the vegetation example since the computational cost associated with the standard $G_r = 1$ based structural solver becomes dominating to that of fluid solver, because of the presence of 3200 flexible filaments. We note that a comprehensive and in-depth exploration of the collective dynamics of the submerged vegetation is outside the scope of the present study and is earmarked for future research. In the following, we describe the advantages of our framework in terms of computational efforts compared to the standard $G_r = 1$ based counterpart. To obtain the results illustrated in this section, the flow solver and interpolation/spreading of different quantities between the two solvers took nearly identical computational time for both the standard $G_r = 1$ and $G_r = 6$ based descriptions.

On the other hand, the $G_r = 6$ based structural solver takes approximately 10.4 times lower computational cost as compared to $G_r = 1$, thereby considerably enhancing the overall efficiency of the FSI simulations. A further investigation reveals that such a reduction in the computational cost for the structural solver with $G_r = 6$ stems from: (i) computations of elemental quantities such as internal force vector, and (ii) solving equations of motion for each filament. The quantitative insights on the computational

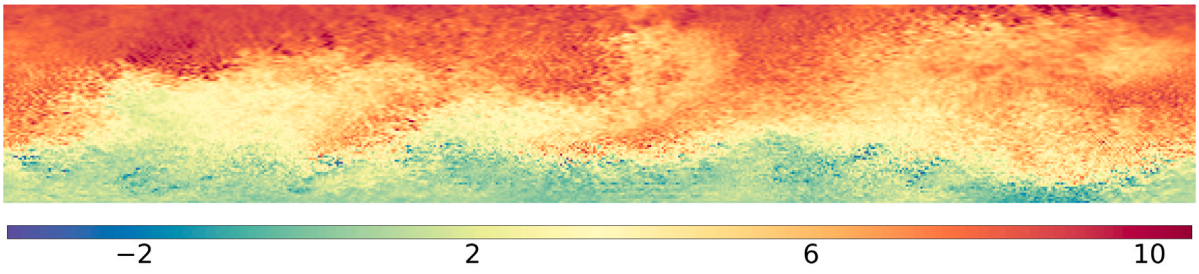

(a) Instantaneous fluid velocity in the streamwise direction on the center plane of the channel at $z = 33$ cm

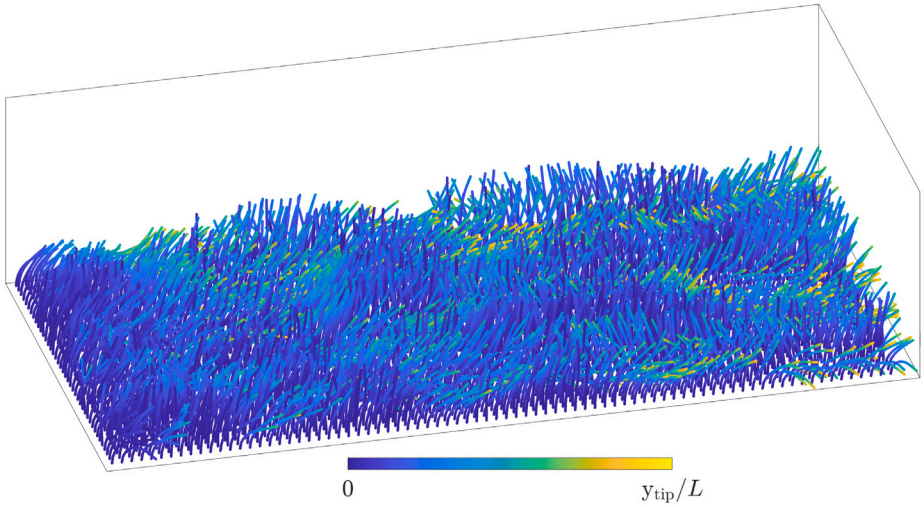

(b) Instantaneous wavelike configurations of the flexible filaments, colored by their absolute deflection from their initial position, throughout the patch

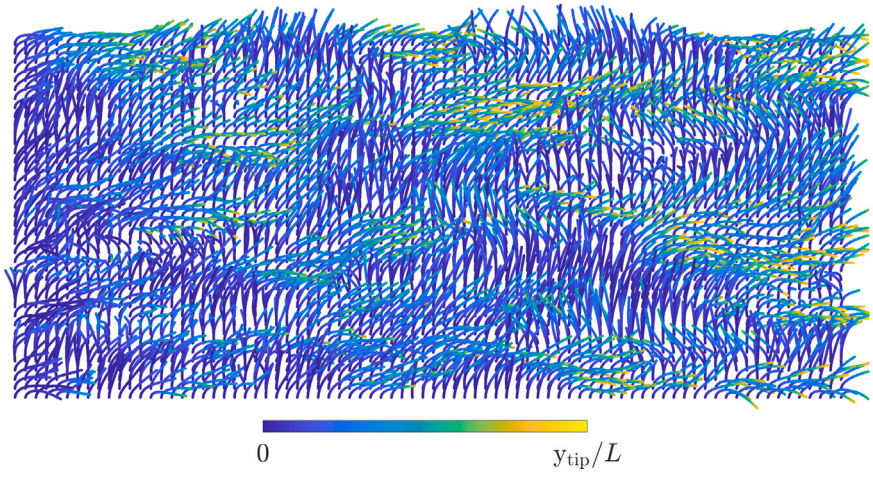

(c) Top view of the instantaneous wavelike configuration of the filaments, colored by their absolute deflection from the initial position throughout the patch

Fig. 22. Snapshots of the streamwise velocity contour and wavelike configurations of the filaments. (For interpretation of the references to colour in this figure legend, the reader is referred to the web version of this article.)

Table 2
Computational efforts associated with the structural solver and its different parts with $G_r = 1$ and $G_r = 6$ based descriptions of the filaments. The structural solver cost with $G_r = 1$ is used as a reference.

	$G_r = 1$ (in %)	$G_r = 6$ (in %)
Structural solver	100	9.64
Elemental quantities	50.16	8.07
System of equations	49.84	1.57

performance of the $G_r = 6$ based structural solver relative to $G_r = 1$ are provided in Table 2. It can be noticed that $G_r = 6$ takes nearly $1/6$ of the computational efforts to compute the elemental quantities. The major gain in efficiency stems from the solution of the governing equations, as 6 times the smaller system of equations is solved in the case of $G_r = 6$ for each filament.

6. Summary

We present a robust and efficient computational framework for fluid–structure interactions of slender flexible filaments in a viscous incompressible fluid. With the objective of accurately computing the elastic responses of filaments exhibiting large deflections/motions due to moderate fluid forces, we adopt the IGA-based implementation of the geometrically exact, nonlinear Cosserat rod formulation. We use the partitioned approach to couple the IGA Cosserat rod-based structural solver with the finite-difference-based fluid solver. A simple yet effective direct-forcing immersed boundary method is employed to transfer the data between the fluid and structure domains. We present a new coupling procedure that overcomes the well-known limitation of the IB method, viz., the local grid density of the structure must be relative to the Eulerian grid to avoid any leakage at the interface. This allows using a much coarser mesh resolution for the immersed NURBS discretized structure than the background flow grid.

We first validate the IGA Cosserat rod-based structural solver using two benchmarks involving large deformations of the flexible beam: bending a cantilever beam and swinging a flexible rod under gravity. We thereafter present the validation of our FSI framework by means of two test cases of increasing complexity: the flapping of a single flexible filament in a uniform flow and an array of flexible filaments subjected to a pulsating flow in a three-dimensional channel. In both cases, the obtained results are in excellent agreement with the numerical and experimental results available in the literature. To explore the IB procedure's performance, the NURBS-discretized filaments' nodal density is systematically varied at a fixed Eulerian grid in both FSI test cases. We show that the proposed procedure allows using at least six times coarser structural meshes than the background fluid grid to attain accurate results without losing numerical stability and robustness, thereby displaying a major gain in computational efficiency. Numerical convergence studies are performed for the first FSI test case, which verifies the proposed framework's consistent performance and second-order convergence rate in space–time. To illustrate the robustness and efficacy of the proposed framework for an application-oriented FSI problem, a submerged vegetation example involving more than 3,000 highly flexible and slender filaments interacting with an incompressible, turbulent flow in a 3D channel is used. Our framework thus allows efficient simulation of such a large-scale FSI problem. In summary, the present framework based on the isogeometric/finite-difference immersed boundary method has proven to be accurate, robust, and efficient for the complex fluid–structure interaction between the flexible filaments and incompressible viscous flow. The ongoing research efforts focus on incorporating the normal and frictional contact between the rod structures and its application to fiber-suspended flows and the paper-making processes.

CRediT authorship contribution statement

Vishal Agrawal: Conceptualization, Methodology, Software, Validation, Formal analysis, Investigation, Data curation, Visualization, Writing – original draft, Writing – review & editing. **Artem Kulachenko:** Conceptualization, Writing – review & editing, Funding acquisition, Supervision. **Nicolò Scapin:** Software. **Outi Tammisola:** Writing – review & editing, Funding acquisition. **Luca Brandt:** Conceptualization, Resources, Software, Writing – review & editing, Funding acquisition, Supervision.

Declaration of competing interest

The authors declare the following financial interests/personal relationships which may be considered as potential competing interests: Vishal Agrawal reports financial support was provided by School of Engineering Sciences, KTH Royal Institute of Technology, Stockholm, Sweden. Outi Tammisola reports financial support was provided by European Research Council.

Data availability

Data will be made available on request.

Acknowledgments

The authors gratefully acknowledge the support from the School of Engineering Sciences, KTH Royal Institute of Technology, Stockholm, Sweden. Vishal Agrawal acknowledges Prof. Artem Korobenko (University of Calgary, Canada) and Dr. Akshay Bhatnagar (IIT Palakkad, India) for the useful discussions, Dr. Arash Alizad Banaei (PDC Center for High Performance Computing, KTH) for providing help related to parallel computing, and Nazario Mastroianni (KTH Mechanics) for help in fixing a bug in FluTAS. Outi Tammisola gratefully acknowledges funding from European Research Council through Starting Grant MUCUS (Grant No. StG-2019-852529). Swedish National Infrastructure for Computing (SNIC) provided high-performance computing and data storage resources.

References

[1] C.F. Schmid, L.H. Switzer, D.J. Klingenberg, Simulations of fiber flocculation: Effects of fiber properties and interfiber friction, J. Rheol. 44 (4) (2000) 781–809, http://dx.doi.org/10.1122/1.551116.
[2] B. Lindström, T. Uesaka, Simulation of the motion of flexible fibers in viscous fluid flow, Phys. Fluids 19 (11) (2007) http://dx.doi.org/10.1063/1.2778937.
[3] J. Zhang, S. Childress, A. Libchaber, M. Shelley, Flexible filaments in a flowing soap film as a model for one-dimensional flags in a two-dimensional wind, Nature 408 (2000) 835–839, http://dx.doi.org/10.1038/35048530.
[4] M.J. Shelley, J. Zhang, Flapping and bending bodies interacting with fluid flows, Annu. Rev. Fluid Mech. 43 (1) (2011) 449–465, http://dx.doi.org/10.1146/annurev-fluid-121108-145456.
[5] H.J.-P. Morand, R. Ohayon, Fluid structure interaction-Applied numerical methods, Wiley, 1995.
[6] E.H. Dowell, K.C. Hall, Modelling of fluid-structure interactions, Annu. Rev. Fluid Mech. 33 (1) (2001) 445–490, http://dx.doi.org/10.1146/annurev.fluid.33.1.445.
[7] N.E. Hussey, S.T. Kessel, K. Aarestrup, S.J. Cooke, P.D. Cowley, A.T. Fisk, R.G. Harcourt, K.N. Holland, S.J. Iverson, S.J. Kocik, J.E.M. Flemming, F.G. Whoriskey, Aquatic animal telemetry: A panoramic window into the underwater world, Science 348 (6240) (2015) 1255642, http://dx.doi.org/10.1126/science.1255642.
[8] H.-J. Bungartz, M. Schäfer, Fluid-Structure Interaction: Modelling, Simulation, Optimisation, Vol. 53, Springer Science & Business Media, 2006.
[9] H.-J. Bungartz, M. Mehl, M. Schäfer, Fluid Structure Interaction II: Modelling, Simulation, Optimization, Vol. 73, Springer Science & Business Media, 2010.
[10] Y. Bazilevs, K. Takizawa, T.E. Tezduyar, Computational Fluid-Structure Interaction: Methods and Applications, John Wiley & Sons, 2013.
[11] P. Causin, J.F. Gerbeau, F. Nobile, Added-mass effect in the design of partitioned algorithms for fluid-structure problems, Comput. Methods Appl. Mech. Engrg. 194 (42) (2005) 4506–4527, http://dx.doi.org/10.1016/j.cma.2004.12.005.
[12] C. Förster, W.A. Wall, E. Ramm, Artificial added mass instabilities in sequential staggered coupling of nonlinear structures and incompressible viscous flows, Comput. Methods Appl. Mech. Engrg. 196 (7) (2007) 1278–1293, http://dx.doi.org/10.1016/j.cma.2006.09.002.
[13] H.J.C. Barbosa, T.J.R. Hughes, The finite element method with Lagrange multipliers on the boundary: circumventing the Babuška-Brezzi condition, Comput. Methods Appl. Mech. Engrg. 85 (1) (1991) 109–128, http://dx.doi.org/10.1016/0045-7825(91)90125-P.
[14] D. Kamensky, M.-C. Hsu, D. Schillinger, J.A. Evans, A. Aggarwal, Y. Bazilevs, M.S. Sacks, T.J.R. Hughes, An immersogeometric variational framework for fluid-structure interaction: Application to bioprosthetic heart valves, Comput. Methods Appl. Mech. Engrg. 284 (2015) 1005–1053, http://dx.doi.org/10.1016/j.cma.2014.10.040.
[15] C. Hirt, A. Amsden, J. Cook, An arbitrary Lagrangian-Eulerian computing method for all flow speeds, J. Comput. Phys. 14 (3) (1974) 227–253, http://dx.doi.org/10.1016/0021-9991(74)90051-5.
[16] W.A. Wall, Fluid-Structure Interaction Based Upon a Stabilized (ALE) Finite Element Method, Sonderforschungsbereich Mehrfeldprobleme in der Kontinuumsmechanik, SFB 404 Stuttgart, 1998, URL https://cir.nii.ac.jp/crid/1574231875329243264,
[17] A.A. Johnson, T.E. Tezduyar, Mesh update strategies in parallel finite element computations of flow problems with moving boundaries and interfaces, Comput. Methods Appl. Mech. Engrg. 119 (1) (1994) 73–94, http://dx.doi.org/10.1016/0045-7825(94)00077-8.
[18] A.A. Johnson, T.E. Tezduyar, 3D simulation of fluid-particle interactions with the number of particles reaching 100, Comput. Methods Appl. Mech. Engrg. 145 (3) (1997) 301–321, http://dx.doi.org/10.1016/S0045-7825(96)01223-6.
[19] T. Sawada, T. Hisada, Fluid-structure interaction analysis of the two-dimensional flag-in-wind problem by an interface-tracking ALE finite element method, Comput. & Fluids 36 (1) (2007) 136–146, http://dx.doi.org/10.1016/j.compfluid.2005.06.007.
[20] A.A. Johnson, T.E. Tezduyar, Numerical simulation of fluid-particle interactions, in: Proceedings of the International Conference on Finite Elements in Fluids, Venezia, Italy., 1995.
[21] A.A. Johnson, T.E. Tezduyar, Advanced mesh generation and update methods for 3D flow simulations, Comput. Mech. 23 (1999) 130–143, http://dx.doi.org/10.1007/s004660050393.
[22] K. Takizawa, T.E. Tezduyar, A. Buscher, S. Asada, Space-time interface-tracking with topology change (ST-TC), Comput. Mech. 54 (2014) 955–971, http://dx.doi.org/10.1007/s00466-013-0935-7.
[23] C.S. Peskin, Flow patterns around heart valves: A numerical method, J. Comput. Phys. 10 (2) (1972) 252–271, http://dx.doi.org/10.1016/0021-9991(72)90065-4.
[24] L. Zhang, A. Gerstenberger, X. Wang, W.K. Liu, Immersed finite element method, Comput. Methods Appl. Mech. Engrg. 193 (21) (2004) 2051–2067, http://dx.doi.org/10.1016/j.cma.2003.12.044, Flow Simulation and Modeling.
[25] L. Zhang, M. Gay, Immersed finite element method for fluid-structure interactions, J. Fluids Struct. 23 (6) (2007) 839–857, http://dx.doi.org/10.1016/j.jfluidstructs.2007.01.001.
[26] T. Rüberg, F. Cirak, Subdivision-stabilised immersed b-spline finite elements for moving boundary flows, Comput. Methods Appl. Mech. Engrg. 209–212 (2012) 266–283, http://dx.doi.org/10.1016/j.cma.2011.10.007.
[27] J. Favier, A. Revell, A. Pinelli, A lattice Boltzmann-immersed boundary method to simulate the fluid interaction with moving and slender flexible objects, J. Comput. Phys. 261 (2014) 145–161, http://dx.doi.org/10.1016/j.jcp.2013.12.052.
[28] F. Xu, D. Schillinger, D. Kamensky, V. Varduhn, C. Wang, M.-C. Hsu, The tetrahedral finite cell method for fluids: Immersogeometric analysis of turbulent flow around complex geometries, Comput. & Fluids 141 (2016) 135–154, http://dx.doi.org/10.1016/j.compfluid.2015.08.027.
[29] C. Kadapa, W.G. Dettmer, D. Perić, A fictitious domain/distributed Lagrange multiplier based fluid-structure interaction scheme with hierarchical B-spline grids, Comput. Methods Appl. Mech. Engrg. 301 (2016) 1–27, http://dx.doi.org/10.1016/j.cma.2015.12.023.
[30] C. Kadapa, W.G. Dettmer, D. Perić, A stabilised immersed framework on hierarchical b-spline grids for fluid-flexible structure interaction with solid–solid contact, Comput. Methods Appl. Mech. Engrg. 335 (2018) 472–489, http://dx.doi.org/10.1016/j.cma.2018.02.021.
[31] A. Nitti, J. Kiendl, A. Reali, M.D. de Tullio, An immersed-boundary/isogeometric method for fluid-structure interaction involving thin shells, Comput. Methods Appl. Mech. Engrg. 364 (2020) 112977, http://dx.doi.org/10.1016/j.cma.2020.112977.

[32] M.C. Wu, H.M. Muchowski, E.L. Johnson, M.R. Rajanna, M.-C. Hsu, Immersogeometric fluid-structure interaction modeling and simulation of transcatheter aortic valve replacement, Comput. Methods Appl. Mech. Engrg. 357 (2019) 112556, http://dx.doi.org/10.1016/j.cma.2019.07.025.
[33] R. Mittal, G. Iaccarino, Immersed boundary method, Annu. Rev. Fluid Mech. 37 (1) (2005) 239–261, http://dx.doi.org/10.1146/annurev.fluid.37.061903.175743.
[34] L.J. Fauci, C.S. Peskin, A computational model of aquatic animal locomotion, J. Comput. Phys. 77 (1) (1988) 85–108, http://dx.doi.org/10.1016/0021-9991(88)90158-1.
[35] L. Zhu, C.S. Peskin, Simulation of a flapping flexible filament in a flowing soap film by the immersed boundary method, J. Comput. Phys. 179 (2) (2002) 452–468, http://dx.doi.org/10.1006/jcph.2002.7066.
[36] Y. Kim, C.S. Peskin, Penalty immersed boundary method for an elastic boundary with mass, Phys. Fluids 19 (5) (2007) http://dx.doi.org/10.1063/1.2734674.
[37] H. Luo, R. Mittal, X. Zheng, S.A. Bielamowicz, R.J. Walsh, J.K. Hahn, An immersed-boundary method for flow-structure interaction in biological systems with application to phonation, J. Comput. Phys. 227 (22) (2008) 9303–9332, http://dx.doi.org/10.1016/j.jcp.2008.05.001.
[38] R. Bhardwaj, R. Mittal, Benchmarking a coupled immersed-boundary-finite-element solver for large-scale flow-induced deformation, AIAA J. 50 (7) (2012) 1638–1642, http://dx.doi.org/10.2514/1.J051621.
[39] J. Lee, D. You, Study of vortex-shedding-induced vibration of a flexible splitter plate behind a cylinder, Phys. Fluids 25 (11) (2013) http://dx.doi.org/10.1063/1.4819346.
[40] H. Dai, H. Luo, J.F. Doyle, Dynamic pitching of an elastic rectangular wing in hovering motion, J. Fluid Mech. 693 (2012) 473–499, http://dx.doi.org/10.1017/jfm.2011.543.
[41] F.-B. Tian, H. Dai, H. Luo, J.F. Doyle, B. Rousseau, Fluid-structure interaction involving large deformations: 3D simulations and applications to biological systems, J. Comput. Phys. 258 (2014) 451–469, http://dx.doi.org/10.1016/j.jcp.2013.10.047.
[42] M.E. Rosti, A.A. Banaei, L. Brandt, M. A., Flexible fiber reveals the two-point statistical properties of turbulence, Phys. Rev. Lett. 121 (2018) 044501, http://dx.doi.org/10.1103/PhysRevLett.121.044501.
[43] A.A. Banaei, M.E. Rosti, L. Brandt, Numerical study of filament suspensions at finite inertia, J. Fluid Mech. 882 (2020) http://dx.doi.org/10.1017/jfm.2019.794.
[44] M. Uhlmann, An immersed boundary method with direct forcing for the simulation of particulate flows, J. Comput. Phys. 209 (2) (2005) 448–476, http://dx.doi.org/10.1016/j.jcp.2005.03.017.
[45] J. Yang, E. Balaras, An embedded-boundary formulation for large-eddy simulation of turbulent flows interacting with moving boundaries, J. Comput. Phys. 215 (1) (2006) 12–40, http://dx.doi.org/10.1016/j.jcp.2005.10.035.
[46] J. Lee, J. Kim, H. Choi, K.S. Yang, Sources of spurious force oscillations from an immersed boundary method for moving-body problems, J. Comput. Phys. 230 (7) (2011) 2677–2695, http://dx.doi.org/10.1016/j.jcp.2011.01.004.
[47] M. Vanella, E. Balaras, A moving-least-squares reconstruction for embedded-boundary formulations, J. Comput. Phys. 228 (18) (2009) 6617–6628, http://dx.doi.org/10.1016/j.jcp.2009.06.003.
[48] M. de Tullio, G. Pascazio, A moving-least-squares immersed boundary method for simulating the fluid–structure interaction of elastic bodies with arbitrary thickness, J. Comput. Phys. 325 (2016) 201–225, http://dx.doi.org/10.1016/j.jcp.2016.08.020.
[49] J.C. Simo, L. Vu-Quoc, A three-dimensional finite-strain rod model. Part II: Computational aspects, Comput. Methods Appl. Mech. Engrg. 58 (1) (1986) 79–116, http://dx.doi.org/10.1016/0045-7825(86)90079-4.
[50] J.C. Simo, L. Vu-Quoc, On the dynamics in space of rods undergoing large motions - A geometrically exact approach, Comput. Methods Appl. Mech. Engrg. 66 (2) (1988) 125–161, http://dx.doi.org/10.1016/0045-7825(88)90073-4.
[51] J.C. Simo, A finite strain beam formulation. The three-dimensional dynamic problem. Part I, Comput. Methods Appl. Mech. Engrg. 49 (1) (1985) 55–70, http://dx.doi.org/10.1016/0045-7825(85)90050-7.
[52] O. Weeger, S.K. Yeung, M.L. Dunn, Isogeometric collocation methods for cosserat rods and rod structures, Comput. Methods Appl. Mech. Engrg. 316 (2017) 100–122, http://dx.doi.org/10.1016/j.cma.2016.05.009.
[53] A. Tasora, S. Benatti, S. Mangoni, R. Garziera, A geometrically exact isogeometric beam for large displacements and contacts, Comput. Methods Appl. Mech. Engrg. 358 (2020) 112635, http://dx.doi.org/10.1016/j.cma.2019.112635.
[54] C. Meier, A. Popp, W.A. Wall, Geometrically exact finite element formulations for slender beams: Kirchhoff-Love theory versus Simo-Reissner theory, Arch. Comput. Methods Eng. 26 (2019) 163–243, http://dx.doi.org/10.1007/s11831-017-9232-5.
[55] T.J.R. Hughes, J.A. Cottrell, Y. Bazilevs, Isogeometric analysis: CAD, finite elements, NURBS, exact geometry and mesh refinement, Comput. Methods Appl. Mech. Engrg. 194 (39–41) (2005) 4135–4195, http://dx.doi.org/10.1016/j.cma.2004.10.008.
[56] J.A. Cottrell, T.J.R. Hughes, Y. Bazilevs, Isogeometric Analysis: Toward Integration of CAD and FEA, Wiley, 2009.
[57] Y. Bazilevs, L. Beirão DA Veiga, J.A. Cottrell, T.J.R. Hughes, G. Sangalli, Isogeometric analysis: approximation, stability, and error estimates for h-refined meshes, Math. Models Methods Appl. Sci. 16 (07) (2006) 1031–1090, http://dx.doi.org/10.1142/S0218202506001455.
[58] J.A. Cottrell, T.J.R. Hughes, A. Reali, Studies of refinement and continuity in isogeometric structural analysis, Comput. Methods Appl. Mech. Engrg. 196 (41) (2007) 4160–4183, http://dx.doi.org/10.1016/j.cma.2007.04.007.
[59] T.J.R. Hughes, J.A. Evans, A. Reali, Finite element and NURBS approximations of eigenvalue, boundary-value, and initial-value problems, Comput. Methods Appl. Mech. Engrg. 272 (2014) 290–320, http://dx.doi.org/10.1016/j.cma.2013.11.012.
[60] L. De Lorenzis, P. Wriggers, T.J.R. Hughes, Isogeometric contact: A review, GAMM-Mitt. 37 (1) (2014) 85–123, http://dx.doi.org/10.1002/gamm.201410005.
[61] V. Agrawal, S.S. Gautam, Varying-order NURBS discretization: an accurate and efficient method for isogeometric analysis of large deformation contact problems, Comput. Methods Appl. Mech. Engrg. 367 (2020) 113125, http://dx.doi.org/10.1016/j.cma.2020.113125.
[62] E. Marino, J. Kiendl, L. De Lorenzis, Isogeometric collocation for implicit dynamics of three-dimensional beams undergoing finite motions, Comput. Methods Appl. Mech. Engrg. 356 (2019) 548–570, http://dx.doi.org/10.1016/j.cma.2019.07.013.
[63] C.S. Peskin, The immersed boundary method, Acta Numer. 11 (2002) 479–517, http://dx.doi.org/10.1017/S0962492902000077.
[64] B.E. Griffith, X. Luo, Hybrid finite difference/finite element immersed boundary method, Int. J. Numer. Methods Biomed. Eng. 33 (12) (2017) e2888, http://dx.doi.org/10.1002/cnm.2888.
[65] S. Tschisgale, J. Fröhlich, An immersed boundary method for the fluid-structure interaction of slender flexible structures in viscous fluid, J. Comput. Phys. 423 (2020) 109801, http://dx.doi.org/10.1016/j.jcp.2020.109801.
[66] A. Suguru, M. Mitsuru, K. Masayuki, S. Kazuhiko, A coupled lattice Boltzmann and cosserat rod model method for three-dimensional two-way fluid-structure interactions, AIP Adv. 11 (7) (2021) http://dx.doi.org/10.1063/5.0058694.
[67] N. Hagmeyer, M. Mayr, I. Steinbrecher, A. Popp, One-way coupled fluid–beam interaction: capturing the effect of embedded slender bodies on global fluid flow and vice versa, Adv. Model. Simul. Eng. Sci. 9 (2022) http://dx.doi.org/10.1186/s40323-022-00222-y.
[68] N. Hagmeyer, M. Mayr, A. Popp, Fully coupled mortar-type embedding of one-dimensional fibers into three-dimensional fluid flow, 2023, arXiv:2306.02456.
[69] S.S. Antman, Nonlinear Problems of Elasticity, second ed., in: Applied Mathematical Sciences, vol. 107, Springer New York, NY, 2005, http://dx.doi.org/10.1007/0-387-27649-1.

[70] J. Mäkinen, Critical study of newmark-scheme on manifold of finite rotations, Comput. Methods Appl. Mech. Engrg. 191 (8) (2001) 817–828, http://dx.doi.org/10.1016/S0045-7825(01)00291-2.
[71] H. Lang, J. Linn, M. Arnold, Multi-body dynamics simulation of geometrically exact cosserat rods, Multibody Syst. Dyn. 25 (2011) 285–312, http://dx.doi.org/10.1007/s11044-010-9223-x.
[72] J.E. Welch, F.H. Harlow, J.P. Shannon, B.J. Daly, The MAC Method-A Computing Technique for Solving Viscous, Incompressible, Transient Fluid-Flow Problems Involving Free Surfaces, Technical report, Scientific Lab., Univ. of California, Los Alamos, 1965, http://dx.doi.org/10.2172/4563173.
[73] J. Kim, P. Moin, Application of a fractional-step method to incompressible Navier-Stokes equations, J. Comput. Phys. 59 (2) (1985) 308–323, http://dx.doi.org/10.1016/0021-9991(85)90148-2.
[74] S. Armfield, R. Street, An analysis and comparison of the time accuracy of fractional-step methods for the Navier–Stokes equations on staggered grids, Internat. J. Numer. Methods Fluids 38 (3) (2002) 255–282, http://dx.doi.org/10.1002/fld.217.
[75] P.R. Spalart, R.D. Moser, M.M. Rogers, Spectral methods for the Navier-Stokes equations with one infinite and two periodic directions, J. Comput. Phys. 96 (2) (1991) 297–324, http://dx.doi.org/10.1016/0021-9991(91)90238-G.
[76] P. Wesseling, Principles of Computational Fluid Dynamics, Vol. 29, Springer Berlin, Heidelberg, 2009, http://dx.doi.org/10.1007/978-3-642-05146-3.
[77] R. Temam, Remark on the pressure boundary condition for the projection method, Theoret. Comput. Fluid Dyn. 3 (1991) 181–184, http://dx.doi.org/10.1007/BF00271801.
[78] P. Costa, A FFT-based finite-difference solver for massively-parallel direct numerical simulations of turbulent flows, Comput. Math. Appl. 76 (8) (2018) 1853–1862, http://dx.doi.org/10.1016/j.camwa.2018.07.034.
[79] M. Crialesi-Esposito, N. Scapin, A.D. Demou, M.E. Rosti, P. Costa, F. Spiga, L. Brandt, Flutas: A GPU-accelerated finite difference code for multiphase flows, Comput. Phys. Comm. 284 (2023) 108602, http://dx.doi.org/10.1016/j.cpc.2022.108602.
[80] N. Li, S. Laizet, 2Decomp&FFT-A highly scalable 2D decomposition library and FFT interface, in: Cray User Group 2010 Conference, 2010, pp. 1–13.
[81] L. Piegl, W. Tiller, The NURBS Book (Monographs in Visual Communication), Springer, Berlin Heidelberg, 2012.
[82] V. Agrawal, S.S. Gautam, IGA: A simplified introduction and implementation details for finite element users, J. Inst. Eng. (India): Ser. C. 100 (3) (2019) 561–585, http://dx.doi.org/10.1007/s40032-018-0462-6.
[83] T.J.R. Hughes, A. Reali, G. Sangalli, Efficient quadrature for NURBS-based isogeometric analysis, Comput. Methods Appl. Mech. Engrg. 199 (5) (2010) 301–313, http://dx.doi.org/10.1016/j.cma.2008.12.004.
[84] F. Auricchio, F. Calabro, T.J.R. Hughes, A. Reali, G. Sangalli, A simple algorithm for obtaining nearly optimal quadrature rules for NURBS-based isogeometric analysis, Comput. Methods Appl. Mech. Engrg. 249–252 (2012) 15–27, http://dx.doi.org/10.1016/j.cma.2012.04.014.
[85] M. Hillman, J.S. Chen, Y. Bazilevs, Variationally consistent domain integration for isogeometric analysis, Comput. Methods Appl. Mech. Engrg. 284 (2015) 521–540, http://dx.doi.org/10.1016/j.cma.2014.10.004.
[86] C. Adam, T. Hughes, S. Bouabdallah, M. Zarroug, H. Maitournam, Selective and reduced numerical integrations for NURBS-based isogeometric analysis, Comput. Methods Appl. Mech. Engrg. 284 (2015) 732–761, http://dx.doi.org/10.1016/j.cma.2014.11.001.
[87] N.M. Newmark, A method of computation for structural dynamics, J. Eng. Mech. Div. 85 (3) (1959) 67–94, http://dx.doi.org/10.1061/JMCEA3.0000098.
[88] A.M. Roma, C.S. Peskin, M.J. Berger, An adaptive version of the immersed boundary method, J. Comput. Phys. 153 (2) (1999) 509–534, http://dx.doi.org/10.1006/jcph.1999.6293.
[89] T. Kempe, J. Fröhlich, An improved immersed boundary method with direct forcing for the simulation of particle laden flows, J. Comput. Phys. 231 (9) (2012) 3663–3684, http://dx.doi.org/10.1016/j.jcp.2012.01.021.
[90] J.H. Lee, B.E. Griffith, On the Lagrangian-Eulerian coupling in the immersed finite element/difference method, J. Comput. Phys. 457 (2022) 111042, http://dx.doi.org/10.1016/j.jcp.2022.111042.
[91] O. Weeger, B. Narayanan, M.L. Dunn, Isogeometric collocation for nonlinear dynamic analysis of cosserat rods with frictional contact, Nonlinear Dynam. 91 (2018) 1213–1227, http://dx.doi.org/10.1007/s11071-017-3940-0.
[92] D.J.J. Farnell, T. David, D.C. Barton, Numerical simulations of a filament in a flowing soap film, Internat. J. Numer. Methods Fluids 44 (3) (2004) 313–330, http://dx.doi.org/10.1002/fld.640.
[93] Z. Y., A DLM/FD method for fluid/flexible-body interactions, J. Comput. Phys. 207 (1) (2005) 1–27, http://dx.doi.org/10.1016/j.jcp.2004.12.026.
[94] I. Lee, H. Choi, A discrete-forcing immersed boundary method for the fluid-structure interaction of an elastic slender body, J. Comput. Phys. 280 (2015) 529–546, http://dx.doi.org/10.1016/j.jcp.2014.09.028.
[95] W.-X. Huang, S.J. Shin, H.J. Sung, Simulation of flexible filaments in a uniform flow by the immersed boundary method, J. Comput. Phys. 226 (2) (2007) 2206–2228, http://dx.doi.org/10.1016/j.jcp.2007.07.002.
[96] A. Pinelli, M. Omidyeganeh, C. Brücker, A. Revell, A. Sarkar, E. Alinovi, The pelskin project: Part IV—control of bluff body wakes using hairy filaments, Meccanica 52 (2017) 1503–1514, http://dx.doi.org/10.1007/s11012-016-0513-0.
[97] E. Murphy, M. Ghisalberti, H. Nepf, Model and laboratory study of dispersion in flows with submerged vegetation, Water Resour. Res. 43 (5) (2007) http://dx.doi.org/10.1029/2006WR005229.
[98] T. Okamoto, I. Nezu, Resistance and turbulence structure in open-channel flows with flexible vegetations, in: Environmental Hydraulics - Proceedings of the 6th International Symposium on Environmental Hydraulics, Vol. 1, (5) 2010, pp. 215–220, http://dx.doi.org/10.1201/b10553-34.
[99] F.-C. Wu, H.W. Shen, Y.-J. Chou, Variation of roughness coefficients for unsubmerged and submerged vegetation, J. Hydraul. Eng. 125 (9) (1999) 934–942, http://dx.doi.org/10.1061/(ASCE)0733-9429(1999)125:9(934).
[100] A. D'Ippolito, F. Calomino, G. Alfonsi, A. Lauria, Flow resistance in open channel due to vegetation at reach scale: A review, Water 13 (2) (2021) http://dx.doi.org/10.3390/w13020116.
[101] M. Maza, J.L. Lara, I.J. Losada, A coupled model of submerged vegetation under oscillatory flow using Navier-Stokes equations, Coast. Eng. 80 (2013) 16–34, http://dx.doi.org/10.1016/j.coastaleng.2013.04.009.
[102] J. O'Connor, A. Revell, Dynamic interactions of multiple wall-mounted flexible flaps, J. Fluid Mech. 870 (2019) 189–216, http://dx.doi.org/10.1017/jfm.2019.266.
[103] S. Tschisgale, B. Löhrer, R. Meller, J. Fröhlich, Large eddy simulation of the fluid–structure interaction in an abstracted aquatic canopy consisting of flexible blades, J. Fluid Mech. 916 (2021) A43, http://dx.doi.org/10.1017/jfm.2020.858.
[104] H. Tariq, U. Ghani, N. Anjum, G.A. Pasha, 3D numerical modeling of flow characteristics in an open channel having in-line circular vegetation patches with varying density under submerged and emergent flow conditions, J. Hydrol. Hydromech. 70 (1) (2011) 128–144, http://dx.doi.org/10.2478/johh-2021-0034.